A Straightforward, One-Step Synthesis of Alkyl Thiol Capped Silver Nanoparticles

A Thesis

Presented to

the faculty of the School of Engineering and Applied Science

University of Virginia

in partial fulfillment

of the requirements for the degree

Master of Science
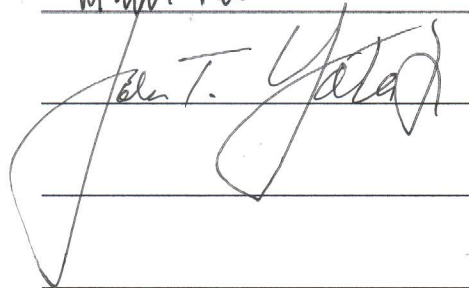
by

Zachary Farrell

August

2012

APPROVAL SHEET

The thesis

is submitted in partial fulfillment of the requirements

for the degree of

Master of Science
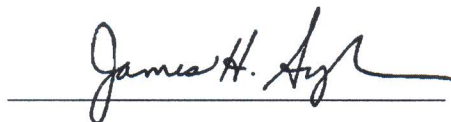

_____

AUTHOR

The thesis has been read and approved by the examining committee:

_____

Advisor

_____

_____

_____

_____

Accepted for the School of Engineering and Applied Science:

_____

Dean, School of Engineering and Applied Science

August

2012

Abstract

Classical nucleation theory and Derjaguin, Landau, Verwey, Overbeek (DLVO) theory for colloidal stability were applied to gain insight into the synthesis of dodecanethiol (DDT)-functionalized silver nanoparticles (NPs) by reduction of silver nitrate with sodium borohydride in ethanol. This analysis indicated the importance of quickly establishing a dense DDT ligand brush on inherently unstable primary particles to achieve colloidal stability. The DLVO calculations also indicated that the electrostatic potential was a minor contributor to repulsive interactions, signifying that it would be possible to control NP size and uniformity in solutions with high ionic strength, as long as sufficient DDT was available to form a densely packed ligand layer on the NPs. These insights were applied to design a new straightforward, one-step, one-phase synthesis for the production of alkyl thiol-functionalized silver NPs. To test the insights from DLVO theory, a battery of 16 samples were synthesized in the parameter space R=3-12, S=1-12 where R=[NaBH$_4$]/[AgNO$_3$], S=[DDT]/[AgNO$_3$], and [AgNO$_3$]=10mM. In general, samples with R=3 or S=1 were polydisperse, however, samples in the R=6-12 and S=3-12 range had uniform particle sizes with average diameters between 3.5-4.7 nm. Additionally, samples with R=72-108 and S=12 were synthesized to test particle stability at high ionic strength; again uniform NPs with average diameters from 3.5-3.8 nm were produced. Ultimately, the insights gained from DLVO theory successfully guided the development of a one-step, one-phase technique for the synthesis of uniform, spherical alkyl thiol-functionalized silver NPs. In future work, this technique will be extended to facilitate the grafting of polymers from phase-separated ligand domains on NP surfaces.

Acknowledgements

There are a number of individuals who deserve recognition and thanks for enabling the work contained in this thesis. First, I would like to thank my advisor, Dr. David Green for humoring my constant skepticism and questions throughout this project; I know so much more now than when we started. I would also like to specifically thank Cameron Shelton, whose assistance in managing the seemingly endless number of nanoparticle syntheses was invaluable. Finally, I would like to thank the members of Dr. Green's research group (current and past) for their help and input: Dan Sunday, Allison Galey, and Caroline Dunn.

Table of Contents

List of Figures

List of Symbols

A_{212} – mixed Hamaker constant for material 2 interacting through medium 1

c/c_0 – supersaturation ratio

C_1 – primary particle concentration

d – surface-to-surface particle separation distance

e – elementary charge

k_B – Boltzmann constant

n – number of monomer units

D – particle diameter

D_{ij} – diffusion coefficient for a particle pair

$\boldsymbol{F}_i^B$ – force on a particle, i, due to Brownian motion

$\boldsymbol{F}_i^c$ – force on a particle due to fluid convection

$\boldsymbol{F}_i^{ex}$ – force on a particle from external sources

$\boldsymbol{F}_i^H$ – force on a particle due to hydrodynamics

$\boldsymbol{F}_i^p$ – force on a particle due to direct interparticle forces

h – dimensionless surface separation, l/d

I – ionic strength

k_r – Smoluchowski aggregation rate constant

k_s – binary aggregation rate constant

l – ligand length

m – particle mass

M_W – ligand molecular weight

N_1 – number concentration of primary particles

N_A – Avogadro's number

$\mathbf{p}_i$ – momentum of a particle, i

r – interparticle distance

P – two-particle probability distribution

R – ratio of sodium borohydride concentration to silver nitrate concentration

s – dimensionless particle surface-to-surface separation distance

S – ratio of dodecanethiol concentration to silver nitrate concentration

t - time

T – temperature

x_i – position coordinate of a particle, i

W – stability ratio, k_r/k_s

$\mathbf{X}$ – the set of position coordinates x_1 and x_2

$\varDelta G$ – free energy of nucleation

β – $(k_B T)^{-1}$

ε – dielectric constant

ζ – Stokes-Einstein friction factor for a sphere

ζ_{ij} – friction coefficient for a particle pair

η_0 – solvent viscosity

κ – inverse Debye length

λ – wavelength

λ_{abs} – wavelength associated with an absorbance peak

λ_{spr} – wavelength associated with a surface plasmon resonanceσ – surface tension

$\mathbf{v}_i$ – velocity of a particle, i

ρ – ligand mass density

τ_b – diffusive or Brownian time scale

υ_{solv} – solvent molar volume

ϕ – ligand volume fraction

Φ_T – total interaction potential

Φ_{VDW} – interaction potential due to Van der Waals forces

Φ_{ELEC} – interaction potential due to electrostatics

Φ_{STERIC} – interaction potential due to steric forces

$\Phi_{OSMOTIC}$ – osmotic contribution to steric interaction potential

$\Phi_{ELASTIC}$ – elastic contribution to steric interaction potential

χ – Flory parameter

Ψ_0 – surface charge

List of Tables

A Straightforward, One-Step Synthesis of Alkyl Thiol Capped Silver Nanoparticles

1. Introduction

The focus of this thesis is to develop a scalable, straightforward, mechanistic, one-step, room temperature, solution-phase method to synthesize spherical, monodisperse, alkanethiol-functionalized silver nanoparticles (NPs). This research will set the stage for our future work in which we will graft polymers from the functional alkanethiol monolayers on metallic nanoparticles via atom transfer radical polymerization (ATRP), a controlled-living polymerization technique to graft polymers, monomer-by-monomer, into polymer brushes. We seek to develop the ligand-functionalized and polymer-grafted nanoparticles for use in nanomaterials that we anticipate will find widespread use in automotive, aerospace, defense, and biomedical applications.[1-5] To realize the production of these materials, it is imperative that we first develop a scalable method to synthesize ligand-functionalized NPs with tunable interfacial properties through control over ligand self-assembly as dictated by number of carbons in the ligand backbone or the types of functional end-groups that affect polymer attachment. Hence, our objective is to develop a facile method to regulate the self-assembly of the ligand monolayer during nanoparticle nucleation and growth.

The motivation for this work is our desire to create platforms of ligand-functionalized NPs that will enable control over the distribution and density of graft polymers on nanoparticle surfaces. Figure 1 gives an illustration of the ligand-functionalized nanoparticles where the dark and light regions represent a homogeneous monolayer of one ligand or a heterogeneous mixture of two chemically distinct ligands that phase-separate on the nanoparticle surface through entropic and enthalpic

interactions on the basis of recent experimental and theoretical studies by Stellacci and co-workers [6-7]
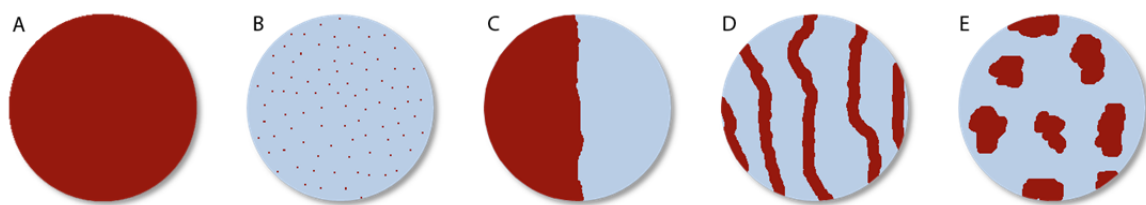
Figure 1: A schematic showing a series of NPs with varying SAMs including homogeneous (composed of either ATRP or inert ligands, A), uniformly mixed monolayer (two ligands distributed randomly, B), Janus particle (two ligands phase-separated by hemisphere, C), striped (two ligands with microphase separation, D), and patchy (two ligands microphase separated, E).

In particular, using gold nanoparticles that vary in size and binary mixtures of alkanethiol ligands that vary in carbon number, Stellacci and co-workers indicate that a combination of entropic and enthalpic interactions govern microphase separation, resulting in uniform ligand mixing (Figure 1b) or the formation of stripes or patches (Figures. 1d and 1e, respectively). In contrast, enthalpic interactions between ligands with poorly mixing functional groups (e.g, $-CH_3$ and $-COOH$) result in bulk, two-dimensional phase separation, leading to the Janus particles in Figure 1c. Recent spectrographic studies by McLean and Cliffel also demonstrate that various mixtures of thiolate ligands yield different degrees of nanophase separation on gold nanoparticles.[8] Moreover, using self-consistent mean-field theory, Egorov modeled ligand de-mixing on the interface of cylinders by varying the Flory parameter, χ, between ligand subunits.[9]

On the basis of these recent publications, our ultimate objective is to create new colloidal building blocks of uniformly-grafted and patchy polymer-grafted nanoparticles by grafting from the phase-separated domains within the two-dimensional ligand shell. To date, patchy polymer-grafted nanoparticles formulated through controlled-living

polymerizations such as ATRP do not exist. While our proposed nanomaterials will be three-orders smaller than the state-of-the art micron-size versions discussed in recent reviews, Kumacheva and coworkers detail in recent publications the three-step synthesis of hydrophilic gold nanorods tethered with hydrophobic, preformed, thiol-terminated polystyrene chains that anchor at the [111] facets at the rod ends.[10] As these nanorods assemble like 'pom-pom' ABA copolymers, researchers refer to the rods as 'pom-pom nanorods'. Unlike Kumacheva who uses a "grafting to" process to attach preformed chains, we will use ATRP, a more flexible, robust "grafting from" technique that permits the formulation of a variety of polymer architectures such as homopolymer, di-block, and tri-block polymer brushes. Researchers grow these structures from the Br atom of tertiary α-bromoester endgroups of ATRP ligands such as that in Figure 2.
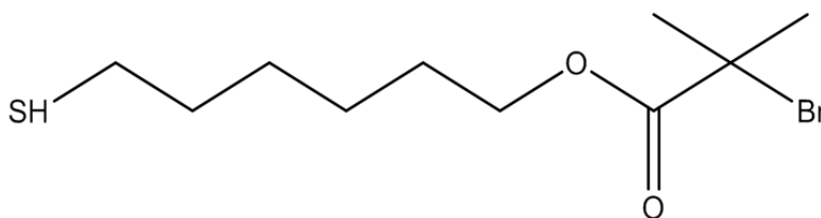
Figure 2: The characteristic α-bromoester functional thiol, 6-mercaptohexyl 2-bromo-2-methylpropanoate. This molecule is a potential initiator for ATRP from Ag nanoparticles.

Further, we seek for the first time to control the polymer chain graft density on small metallic nanoparticles by grafting from a uniform distribution of ATRP ligands, or active ligands, as illustrated in Figure 1b. This will enable the formulation of polymer-grafted nanoparticles that mimic star polymers by replacing the organic core with a metallic one that becomes a single branch point from which linear chains (or arms) emanate. Hence, our work will expand the range of graft densities on small metallic cores for "grafting from" techniques that yield high graft densities (e.g., ~1 chain/nm^2) by

reducing the graft density, and thereby increasing the range that researchers can tune nanoparticle interactions in soft materials.[11-14]

The first step in making the uniformly grafted and patchy polymer-grafted nanoparticles is to develop a scalable, one-step, one-phase, room temperature synthesis to make spherical, monodisperse alkyl thiol functionalized Ag nanoparticles, which is the objective of this thesis. Despite the fact that the chemistry of noble metal nanoparticles has been a research topic of interest since Faraday's work with gold sols, we chose this objective as the literature contains very few mechanistic approaches on the synthesis of ligand-functionalized nanoparticles in bulk solution at room temperature. Hence, we endeavor to fill this void with a rationally-designed, mechanistic approach to avoid special, ad-hoc treatments of the reaction system such as the dropwise addition of reagents or the unnecessary chilling or heating of solutions.[7] For our initial studies, we have selected Ag as the material of choice, as it is significantly more affordable than Au and synthetic development is likely to require a significant amount of material expenditure. In our approach we seek to regulate the self-assembly of the ligand monolayer during the nucleation and growth of Ag nanoparticles during reduction of a silver nitrate ($AgNO_3$) with sodium borohydride ($NaBH_4$). A study of the factors that control reaction kinetics and mass transfer has led us to hypothesize that we can exert mechanistic control over the nanoparticle synthesis through manipulation of three key parameters: the concentration of silver nitrate, the concentration of reducing agent, R, and the concentration of dodecanethiol, S. We select dodecanthiol (DDT) as the model ligand for our studies as it is highly miscible with ethanol, less hazardous than many other thiols, liquid at room temperature, and non-volatile. Though we are beginning our studies

with DDT, it is very likely this method can be generalized to the production of thiol functionalized nanoparticles, as long as the ligand of interest is soluble in ethanol. For example, by choosing an appropriate mixture of two ligands, we expect to be able to extend this synthetic technique to the production of nanoparticles with varying brush layer morphologies, such as the uniformly mixed, patchy, and fully-phase separated or Janus particles which appear in Figure 1.

2. Background, Theory, and Objectives

In this section we provide the background and theory to support our hypothesis and objectives in the development of the DDT-functionalized Ag nanoparticles. In Section 2.1 we discuss the state-of-the-art methods to synthesize Ag nanoparticles and provide the rationale for our initial research efforts. Subsequently in Sections 2.2-2.4 we give a heuristic treatment of nanoparticle nucleation and a theoretical treatment of nanoparticle growth which involves respectively a discussion of classical nucleation theory and Smoluchowski aggregation kinetics for colloidal systems. Woven into the discussion is a review of fundamental studies on the nucleation and growth of Ag and Au nanoparticles in bulk solutions as well as theoretical calculations from which we develop hypotheses in Section 2.5 and discuss how the concentrations of Ag salt, reducing agent, and dodecanethiol (DDT) control nanoparticle growth. In the final subsection (Section 2.6) we provide the objectives for this thesis.

2.1 Current State of the Literature in the Area of Silver Nanoparticle Synthesis

Since nanoparticle synthesis is the first step towards the production of metallic nanoparticles with phase-separated oligomeric brushes domains for polymer-grafting, it is imperative that the synthetic method serve as a platform technology for all of the derivative research. In light of this, a comprehensive review of the literature is essential to elucidate the rationale for selecting a sufficiently robust method for nanoparticle synthesis. As the volume of literature in this area was recently described by Zukoski, a key researcher on the growth mechanisms of noble metal nanoparticle, as "staggering",[15] it is necessary to color our discussion by first enumerating the criteria essential to our

selection of a synthesis amenable to the future goal of grafting polymers from phase-separated oligomeric domains on Ag nanoparticles. To meet our minimal needs, a synthesis must produce spherical, uniform, Ag nanoparticles near the reported primary particle diameter of 2 nm.[16] It must also be a versatile, one-phase method that works well with a range of alkanethiol ligands and straightforward in its methods for production and purification of the resultant nanoparticles. In light of these specific needs, we identified three prevalent synthetic methods: 1) the Brust-Schiffrin synthesis;[17] 2) the citrate method;[18] and 3) one-phase reduction with sodium borohydride.[15,16] We discuss these methods below and select the synthesis that best fits our needs.

The first method, the Brust-Schiffrin synthesis, is a two-phase, surfactant-templated method that involves the use of a water-in-oil microemulsion in which a cationic surfactant (e.g., tetraoctylammonium bromide) forms inverted micelles containing water in toluene. The micelles function as nano-reactors within which the nanoparticles grow from the reduction of a water-soluble metal salt (e.g., $AgNO_3$) by a reducing agent (e.g., $NaBH_4$). The cationic surfactant stabilizes the nanoparticles against aggregation until functionalization by dodecanethiol from the toluene phase. While the resultant nanoparticles are small, having diameters of between 1-3 nm, obtaining purely dodecanethiol-functionalized nanoparticles is difficult due to competitive adsorption of the cationic surfactant.[7,17] The Brust-Schiffrin synthesis therefore does not meet our need for a one-phase method which is straightforward with respect to nanoparticle purification.

The second synthesis, the citrate method, is a one-phase synthesis in which citric acid reduces $AgNO_3$ in hot ethanol.[18] In general, this method produces uniform, spherical particles of ~7.5 nm in diameter. Though the method offers advantages such as

environmentally benign reagents and scalable production, the sizes achieved are larger than ideal for our purposes. Purity of the resultant nanoparticles is also potentially an issue, as citrate may be competitive with dodecanethiol for adsorption to the nanoparticle surface, impeding the formation of our desired oligomeric brush. In light of this information, the citrate method does not meet our needs for a nanoparticle synthesis.

The third general class of methods, syntheses employing one-phase reduction of noble metals by $NaBH_4$ in protic solvents, is ultimately what we settled on as the basis for our synthetic procedure. The common thread running through the methods in this category is that in all cases, $NaBH_4$ is the reducing agent and the synthesis is carried out without a need for phase transfer (i.e., growth in microemulsion templates). In contrast, for our purposes, Ag^+ in the form of $AgNO_3$ is directly reduced by $NaBH_4$ in ethanol. Although the method is straightforward as it is easy to add a metal salt and $NaBH_4$ to protic solvents, controlling particle growth is challenging which has led to a number of ad-hoc protocols. Some of the most commonly occurring variations include dropwise addition of reagents,[7] pre-treatment of $AgNO_3$ with NH_3 to produce a Tollens-like reagent before reduction with $NaBH_4$,[19] emphasis on temperature control,[15] and addition of thiol ligand directly to the Ag salt, incurring the formation of metal-thiolates.[20,21]

Hence, we base our procedure on the findings of recent mechanistic studies of the $NaBH_4$ synthesis, which lead us to conclude that it provides the best platform to produce uniform particles close to the primary particle size.[16] We also conclude that the various ad-hoc protocols to synthesize alkane-functionalized metallic nanoparticles with the $NaBH_4$ method do not take into account the physical underpinnings of nanoparticle nucleation and growth. In light of this, we found it necessary to develop a rational and

scalable synthetic scheme based on nanoparticle growth mechanisms to avoid *ad-hoc* treatments without insight into their effects on particle formation.

To this end, the foundation of our work stems from the studies of Zukoski et al. and Polte et al.[15,16] Zukoski published the first mechanistic studies that link both the nucleation and growth of Au and Ag nanoparticles in bulk solution to predict the time-dependent evolution of the particle size.[15,22] Strongly influenced by these investigations, Polte followed with recent small-angle x-ray scattering studies to quantify the size of the nuclei, or primary particles, and their subsequent growth.[16] Both groups of researchers concur that subsequent to the initial and rapid (~ 100 ms) reduction of the metal precursor, nuclei form with diameter, $D \approx 2$ nm, that then grow through aggregation controlled by Brownian motion and particle interactions until reaching a stable size.

We contend that the separation between the length and time scales of nucleation and growth provide opportunities to perfect the synthesis of spherical, DDT-functionalized Ag nanoparticles. Our synthetic protocol in Figure 6 in Chapter 3 illustrates the mixing of two vials, the first containing $AgNO_3$ and the second $NaBH_4$ and dodecanethiol, in which separating $AgNO_3$ from dodecanethiol mitigates the undesirable formation of Ag(I)-thiolates. On the basis of the analysis in this Chapter below, mixing of the two streams in Figure 6 enables the fast reduction of Ag^+ to Ag^0 on molecular length and time scales, 1-9 Å and 10^{-13}s, respectively, resulting in nuclei formation. Subsequently, the aggregative growth of primary particles in the presence of 1 nm-sized dodecanethiol molecules ensues within the colloidal domain (1nm–1μm), resulting in a clear separation in time from nucleation, not only through slower diffusion, but also though hydrodynamic interactions from frictional forces on the nanoparticles and the

alkanethiols from the surrounding solvent. Hence, we review the theories of nuclei formation and colloidal aggregation to gain insight into how the concentrations of the metal salt, reducing agent, and dodecanethiol ligand impact Ag nanoparticle formation. We subsequently formulate our hypotheses and the objectives of this thesis based on the analysis of our particle interaction potential calculations.

2.2 Nucleation of Primary Particles

An analysis of classical nucleation theory is a starting point for shedding light on how the reaction chemistry impacts the formation of primary particles during the synthesis of the DDT-functionalized Ag nanoparticles.[18] According to the theory, nucleation occurs when the concentration, c, of reduced metal precursors, i.e., Ag^0, crosses a saturation value, c_0, after which the precursor concentration decreases rapidly as primary particles form.[23] The proposed net reaction for the reduction of Ag^+ by BH_4^- in ethanol is,[24,25]

$$2Ag^+ + 2BH_4^- + 6CH_3CH_2OH \rightarrow 2Ag^0 + 7H_2 + 2B(OCH_2CH_3)_3. \tag{1}$$
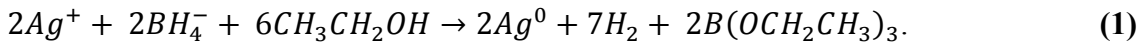
According to Polte and coworkers, the reduction of Ag^+ to Ag^0 is rapid, with all ionic silver being reduced to elemental silver within the first 100 ms. This rapid jump in Ag^0 leads directly to nuclei formation through the transfer of a number of n Ag^0 species from solution into a primary particle of diameter, D, as characterized by the free energy of nucleation, ΔG, in Eq. 2.

$$\Delta G = -nk_B T \ln\left(\frac{c}{c_0}\right) + \pi D^2 \sigma \tag{2}$$

The driver for nucleation in Eq. 2 is the supersaturation ratio, c/c_o, while the opposition to nucleation is the far right hand term that represents the surface energy from the surface tension, σ, between the solvent and primary particle which must be overcome to form nuclei. Nucleation occurs when $c/c_o > 1$, and Polte and coworkers indicate that the primary particle diameter is $D \approx 2$ nm.[12]

Assuming that the Ag^0 species is in equilibrium with a bath of solvent molecules, one can derive a nucleation rate using Fick's first law of diffusion in Eq. 3,[26]

$$\frac{dN_1}{dt} = k_r c^2 \exp\left(\frac{-\Delta G^*}{k_B T}\right)$$

(3)

where ΔG^* is the free energy of nucleation at a given nucleus size and k_r is the diffusion-limited binary rate constant, also termed the Smoluchowski aggregation rate constant, which we derive in Eq. 21 in the next section.

Eq. 3 is our starting point for insight into how the reaction chemistry impacts the rate of nucleation during the synthesis of the DDT-functionalized Ag nanoparticles. The nucleation rate should be as low as possible to slow the rate of primary particle aggregation to provide more time for functionalization of each nuclei during synthesis. The activation barrier, the exponential in Eq. 3, should remain relatively constant due to the unchanging value of the surface energy term in Eq. 2 consistent with the formation of same-sized nuclei in ethanol. Thus, lowering the nucleation rate translates into reducing the concentration of Ag^0, or c, in Eq. 3 which stems from the reduction of Ag^+ in Eq. 1 that derives from the dissociation of a lower [$AgNO_3$] in solution. Hence, [$AgNO_3$] should be as low as possible, and to this end, we select [$AgNO_3$]=10 mM, a low value consistent with previous studies.[19,24] Moreover, we select $NaBH_4$ levels that are at least

three times those of $AgNO_3$ based on the findings of Zukoski and coworkers who indicate

that the reaction in Eq. 2 requires this level of excess of reducing agent to drive reduction

and nucleation.[15]

2.3 Theory of Aggregative Particle Growth

Subsequent to nucleation, the primary particles experience growth; on the basis of

studies by Zukoski and Polte, growth occurs through controlled aggregation, or the

aggregation of primary particles into doublets, triplets, etc., ultimately reaching a stable

size based on particle interactions.[16,22] The starting point for the analysis of particle

aggregation is the generalized Smoluchowski diffusion equation (GSE), characterizing

the dynamics of a system of N colloidal objects (e.g, sphere, rods, cubes, etc.). Our

objective is to use the theory to elucidate the reaction conditions that facilitate the end-on

adsorption of alkanethiol monolayers on primary particles, mitigating aggregation. Based

on the terminology in the soft matter field, the oligomeric self-assembled alkanethiol

monolayer (SAM) forms a "brush" on the nanoparticle surface.[27,28] A brush results from

the stretching of densely packed, end-tethered oligomers or polymers that form an end-

tethered 3-D monolayer on a 2-D surface. Using brushes to stabilize particles result in

"colloidal stability" through "steric stabilization". Monographs on these phenomena have

been published by Napper and Russel, Saville, and Schowalter.[29,30]

The objective of applying the GSE to the kinetics of aggregation is to predict the

rate at which primary particles disappear, by colliding to form doublets, triplets, and

larger aggregates. Hence, the GSE provides the basis of population balance and Brownian

dynamics models for addressing the dynamics of a variety of colloidal phases (e.g.,

macromolecules, emulsions, aerosols, foams, etc.)[31] We present the following derivation

in real-space coordinates to correspond with our use of transmission electron microscopy,

a direct visualization method to image the DDT-functionalized Ag nanoparticles.

The starting points for the derivation of GSE are Eqs. 4, 5, and 6. Eq. 4 is the

probability conservation equation for $P(\mathbf{x_1}, \mathbf{x_2}, t)$, or the pair, or two-particle probability

distribution function (PDF), which characterizes the stochastic, time-dependent, spatial

arrangement of nanoparticles at positions $\mathbf{x_1}$ and $\mathbf{x_2}$ relative to the average position of an

assembly of the other N-2 spheres. For convenience, we represent $\mathbf{x_1}$ and $\mathbf{x_2}$ as the set of

position coordinates, X, and bold text represents vector quantities.

$$\frac{\partial P(X,t)}{\partial t} + \sum_{i=1}^{N} \nabla \cdot \left(v_i(X) P(X,t) \right) = 0 \tag{4}$$

Eq. 4 is a familiar mass balance equation to quantify the accumulation and flux of

particles in and across an arbitrary control volume, where v_i is velocity of particle i. Eq. 5

is Newton's equation of motion for particle i, otherwise called the Langevin equation as it

accounts for particle diffusion through Brownian motion:

$$\frac{d\mathbf{p}_i}{dt} = \sum_i \mathbf{F}_i = \mathbf{F}_i^p + \mathbf{F}_i^{ex} + \mathbf{F}_i^H + \mathbf{F}_i^B + \mathbf{F}_i^c \tag{5}$$

where $\mathbf{p}_i$ is the momentum of particle i which equals $\mathbf{p}_i = m\mathbf{v}_i$ where m is the particle

mass. On the left hand side of Eq. 5 is the summation of the forces acting on the particle

where $\mathbf{F}_i^p$ is due to direct interparticle forces, $\mathbf{F}_i^{ex}$ to external forces (e.g., gravity), $\mathbf{F}_i^H$ to

the hydrodynamic force by the surrounding fluid, $\mathbf{F}_i^B$ to Brownian motion, which drives

particle diffusion, and $\mathbf{F}_i^c$ fluid convection. By definition, the position coordinate, x_i, of

the particle relates to the momentum coordinate in Eq. 6 as:

$$\frac{dx_i}{dt} = \frac{p_i}{m} \tag{6}$$

Eqs. 4-6 provide the basis for addressing a variety of dynamic colloidal processes such as suspension rheology or aerosol transport. Russel, Saville, and Schowalter and Dhont provide a full treatment and application of these relations to colloidal processes.[30,32]

Knowledge of the reaction conditions permits a number of simplifications to Eq. 4-6 to model the early stage growth of a dilute suspension of hydrodynamically non-interacting Ag nanoparticles in an unbounded, quiescent solvent without the influence of external fields. Growth in a quiescent solution dictates a lack of fluid convection, or F_i^c =0, and that particle movement through Brownian motion occurs at low Reynolds number, i.e., the ratio of inertial to viscous forces, where viscous forces dominate inertial ones. Particle growth from a dilute suspension permits the assumption that particle motions and collisions occur on time scales much greater than the diffusive, or Brownian time scale of $\tau_b \approx 10^{-9}$s.[30,32] We anticipate that after nucleation, collisions between primary particles should occur on a time scale of $t > 10^{-3}$s thus, $t \gg \tau_b$.[22,30,32] The time scale τ_b corresponds to the translational momentum relaxation time; thus at $t \gg \tau_b$, the particles experience quasi-inertia free motion, reaching a constant velocity, which sets $d\mathbf{p}_i/dt=0$ in Eq. 5.[30,32] This simplifies further analysis that depends only on position coordinates since velocities can be calculated from Eq. 6. Moreover, setting $d\mathbf{p}_i/dt=0$ yields a force balance between the hydrodynamic, Brownian, and direct particle interaction terms in Eq. 7 as F_i^{ex} =0,

$$F_i^H = -\left(F_i^p + F_i^B\right) \tag{7}$$

since we assume that particle sedimentation is negligible at the early stages.

Determination of the GSE requires calculation of the particle velocity from the hydrodynamic force, the latter of which depends on a phenomenological treatment of solvent motion where processes on the molecular level are not considered. Thus, only macroscopic properties such as the viscosity and mass density of the solvent enter into the analysis. The large difference in relevant length and time scales of momentum relaxation between the solvent and the ensemble of primary particles facilitates the phenomenological treatment of hydrodynamics in colloidal systems without losing the microstructure of the nanoparticle arrangements.[32,33] To this end, the hydrodynamic force on particle i by the surrounding fluid in shown in Eq. 8 and the generalized hydrodynamic Stokes-Einstein relation is given in Eq. 9; both equations provide the starting point for incorporating hydrodynamics in early stage nanoparticle growth:

$$\boldsymbol{F}_i^{H} = -\sum_{j=1}^{N} \zeta_{ij}(\boldsymbol{X}) \cdot \boldsymbol{v}_j \tag{8}$$

$$\sum_{j=1}^{N} \zeta_{ij}(\boldsymbol{X}) \cdot \boldsymbol{D}_{ij}(\boldsymbol{X}) = k_b T \delta_{ij} \mathbf{1} \text{ or } \zeta(\boldsymbol{X}) \cdot \boldsymbol{D}(\boldsymbol{X}) = k_b T \mathbf{1} \tag{9}$$

where ζ_{ij} and D_{ij} are the friction and diffusion coefficients for the particle pairs. One adds the minus sign in Eq. 8 to account for the force exerted by the fluid on the particle. For the case of interacting particles in a concentrated suspension, the friction coefficients form a real, symmetric, positive definite $3N$ x $3N$ matrix that depend on particle position, resulting in a non-symmetric matrix of microscopic diffusion coefficients due to the inversion of the friction coefficients in Eq. 9. For a dilute suspension of hydrodynamically non-interacting primary particles, the friction coefficient and diffusion matrices become diagonal in Eq. 10 and factor to a scalar value D_o, in Eq. 11, resulting in linear relationship between $\mathbf{v}_i$ and $\boldsymbol{F}_i^{H}$:

$$\boldsymbol{D}_{ij}(\boldsymbol{X}) = D_o \delta_{ij} \boldsymbol{1} \tag{10}$$

$$\boldsymbol{v}_i(\boldsymbol{X}) = -\sum_{j=1}^{N} \beta \boldsymbol{D}_{ij}(\boldsymbol{X}) \cdot \boldsymbol{F}_j^H = -\beta D_o \boldsymbol{F}_i^H = -\zeta^{-1} \boldsymbol{F}_i^H = -\boldsymbol{F}_i^H / 6\pi\eta_o R \tag{11}$$

where $\beta = (k_b T)^{-1}$ and ζ is the well known Stokes-Einstein friction factor for spheres equal to $6\pi\eta_o R$ where η_o is the solvent viscosity and R the particle radius.

Substituting Eqs. 7 and 10 into Eq. 4 yield the GSE for the primary particles in Eq. 12:

$$\frac{\partial P(\boldsymbol{X},t)}{\partial t} + \beta D_o \sum_{i=1}^{N} \nabla_i \cdot \left[\left(\boldsymbol{F}_i^p + \boldsymbol{F}_i^B \right) P(\boldsymbol{X},t) \right] = 0 \tag{12}$$

which can be further clarified by considering the direct interparticle and Brownian forces, or $\boldsymbol{F}_i^p$ and $\boldsymbol{F}_i^B$, respectively. Calculation of direct interparticle forces stems from the gradient of the total potential energy $\Phi_T(\boldsymbol{X})$ of the ensemble of primary particles which is a function of the position coordinates in Eq. 13.

$$\boldsymbol{F}_i^p = -\nabla \Phi_T(\boldsymbol{X}) = -\sum_{j=1}^{N} \nabla_i \Phi_T(x_{ij}) \tag{13}$$

The basis for the Brownian force stems from the establishment of equilibrium at long times where the PDF is proportional to the exponential of the Boltzmann distribution:[5]

$$\lim_{t \to \infty} P(\boldsymbol{X},t) \sim \exp(-\beta \Phi_T(\boldsymbol{X})) \tag{14}$$

and the terms in within the round brackets in Eq. 12 becomes zero for the particular form of the PDF in Eq. 14. From this requirement, one finds the form of the Brownian force in Eq. 15.

$$\boldsymbol{F}_i^B = -k_B T \nabla_i \ln P(\boldsymbol{X},t) \tag{15}$$

Substitution of Eqs. 13 and 15 into Eq. 12 yield the GSE in Eq. 16 for the primary particles,

$$\frac{\partial P(X,t)}{\partial t} = D_o \sum_{i=1}^{N} \nabla_i \cdot \left[(\nabla_i + \beta \nabla \Phi_T(X))\right] P(X,t) \qquad (16)$$

The GSE forms the basis of our analysis of the reaction conditions that control the early stage growth of the DDT-functionalized Ag nanoparticles. To quantify singlet-to-doublet formation, one derives the conservation equation for the primary particle concentration, C_1, by multiplying Eq. 4 by $1/(N-1)$ integrating over the position of N-1 spheres. The derivation requires the tracking of doublet formation upon primary particle overlap, corresponding to $P(X,t)=0$ for the interparticle distance $r_{ij}=|x_1-x_2|<2R$ for $i\neq j$. The analysis of the integrals over the remaining volume is found in Russel, Saville, and Schowalter who use the transport and divergence theorems to determine the rate of change of C_1,

$$\frac{dC_1(t)}{dt} = - \int_{r=2R} P(X,t) \cdot \mathbf{n} dr \qquad (17)$$

where $C_1 = C_{1,0}$ at t=0.[25] Hence, the disappearance rate of primary particles depends on $P(X,t)$, which can be determined assuming pseudo-steady state and spherically-symmetric direct pair interactions, $\Phi(r)$, reducing Eq. 17 to,

$$\frac{D_o}{r^2} \frac{d}{dr} r^2 \left(P \frac{d(\beta \Phi_T)}{dr} + \frac{dP}{dr} \right) = 0 \qquad (18)$$

subject to the following boundary conditions:

$$P(r) = \begin{cases} C_1^2 & r \to \infty \\ 0 & r = 2R \end{cases} \qquad \textbf{(BC 1)}$$

The former assumes a random, spatially homogenous particle arrangement, or microstructure, and the latter doublet formation. Integration and application of the boundary conditions yields:[30]

$$P(r) = C_1^2 \frac{\exp(-\beta\Phi_T)\int\limits_{2R}^{r}\exp(\beta\Phi_T)r^{-2}dr}{\int\limits_{2R}^{\infty}\exp(\beta\Phi_T)r^{-2}dr} \tag{19}$$

The primary particle disappearance rate follows from Eq. 17 as,

$$\frac{dC_1(t)}{dt} = -\frac{4k_BT}{3\eta_oR}\frac{C_1^2}{\int\limits_{2R}^{\infty}\exp(\beta\Phi_T)r^{-2}dr} = -k_sC_1^2 \tag{20}$$

where k_s is the binary aggregation rate constant.

On the basis of Eq. 20 the prevention of the aggregation of primary particles requires a lowering of its concentration, C_1, which occurs through using a low [AgNO$_3$], as well as a strong reduction in k_s, which depends on the thermal and transport properties of the solvent, T and η_o, respectively, and particle interactions through Φ_T. The parameter k_s does vary with particle size; however, we hold it constant in our analysis at $D\approx2$ nm on the basis of recent small-angle x-ray scattering studies.[16] While reducing T would slow aggregation, controlling particle interactions should have a larger effect due to the exponential dependence of k_s on Φ_T. To elucidate this dependence, a useful estimate is the stability ratio, $W=k_r/k_s$, as it is convenient measure of the impact of Φ_T on k_s though comparison of k_s to the maximum, diffusion-limited rate of doublet formation, k_r. otherwise known as the Smoluchowski aggregation rate.[34] One approximates k_r by setting $\Phi_T=0$, indicative of a balance between attractions and repulsions between nanoparticles, yielding Eq. 21,

$$k_r = \frac{8k_B T}{3\eta_o} \tag{21}$$

which one substitutes into W to produce Eq. 22,

$$W = \frac{k_r}{k_s} = 2R \int_{2R}^{\infty} \exp(\beta\Phi_T)r^{-2}dr = \int_0^{\infty} \exp(\beta\Phi_T)(s+2)^{-2}ds \tag{22}$$

where $\underline{s}$ is the dimensionless particle surface-to-surface separation distance

$$s = \left(\frac{r}{R} - 2\right) \tag{23}$$

Hence, interparticle interactions dictate the value of W which typically ranges between 1-10^5.[34] Diffusion-limited aggregation and highly unstable particles occur at the lower limit at $W \approx 1$ when particle attractions typically through van der Waals forces overwhelm particle repulsions. In contrast, the upper limit at $W \sim 10^5$ corresponds to high interparticle repulsion energies, e.g., 10-20 $k_B T$, and very stable primary particles. Hence, control over interparticle repulsions is essential to achieving the objective of a scalable, mechanistic, one-step synthesis of DDT-functionalized Ag nanoparticles. In the next section, we examine the interparticle interaction potentials relevant to the production of primary particles through the reduction of $AgNO_3$ by $NaBH_4$ and the subsequent functionalization by DDT through application of Derjaguin, Landau, Verwey, Overbeeek (DLVO) theory for colloidal stability.[23,34,35-37] This analysis will lead to our hypotheses and objectives for the design of a straightforward, scalable synthesis of alkanethiol functionalized Ag nanoparticles.

2.4 Development of Interparticle Potentials for Aggregative Growth

Subsequent to the derivation of the stability ratio, W, it is necessary to delve into the individual components which make up the net interaction potential. For the reduction of $AgNO_3$ by $NaBH_4$ leading to the formation of nanoparticles that are subsequently functionalized by DDT, we expect contributions to the interparticle potential from Van der Waals (VDW), electrostatic, and steric interactions. The development of the electrostatic potential stems from early investigations on the role of the electrolyte on colloidal destabilization;[38-41] however, a theory to accurately describe this behavior did not become available until the development of colloidal potentials for attractive and repulsive Van der Waals and electrostatic interactions, respectively. These derivations were carried out by Derjaguin and Landau (1941) and Verwey and Overbeek (1948), resulting in DLVO theory.[42,43] This theory has been further extended to aggregation of unlike particles via Brownian motion and shear-induced flocculation.[44,45]

The electrostatic potential does not represent the sole barrier to aggregation during particle growth in the presence of dodecanethiol; the end-tethered adsorption of dodecanethiol ligands also provides colloidal stability via steric repulsion. Vincent and coworkers developed the first widely used model for steric repulsion in 1986.[46] They subdivide steric repulsion into osmotic and elastic contributions, with the osmotic portion being due to the energy expenditure required force a solvent from an oligomeric brush upon the overlap and interpenetration of the brushes on two particles. The elastic portion is due to the energy needed to compress oligomeric brush upon nanoparticle contact. Based on the work of Derjaguin, Landau, Verwey, Overbeek, and Vincent, we develop

the interparticle pair potential, Φ_T, for substitution into Eq. 22 to elucidate the stability of the primary particles.

The pairwise (two-body) net interaction potential, Φ_T, is shown in Eq. 24

$$\Phi_T = \Phi_{VDW} + \Phi_{ELEC} + \Phi_{STERIC} \tag{24}$$

which is the sum of the attractive van der Waals (VDW) interactions, Φ_{VDW}, as well as the repulsive electrostatics and steric interactions, Φ_{ELEC} and $\Phi_{STERIC.}$

The van der Waals contribution was calculated assuming two equally-sized spherical primary particles with high radius of curvature, which causes Φ_{VDW} to take the form in Eq. 25.

$$\Phi_{VDW} = -\frac{A_{212}}{6}\left[\frac{D^2}{2d^2 + 4Dd} + \frac{D^2}{2d^2 + 4Dd + 2D^2} + \ln\left(\frac{d^2 + 2Dd}{d^2 + 2Dd + D^2}\right)\right] \tag{25}$$

The term in brackets accounts for particle geometry, with this particular representation for spheres of high curvature. In the bracketed term, D is the particle diameter, d the surface-to-surface particle separation distance. The other quantity of note in Eq. 25 is A_{212}, the mixed Hamaker constant for particles of material 2 interacting through medium 1, which is calculated from the geometric mean of the individual Hamaker constants listed in Table 1. The Hamaker constant is a material property representative of the strength of Van der Waals attractions between colloids; this constant is calculated by summing pairwise over interactions between atoms in the materials. For metals, this constant is large (~100 $k_B T$ for silver) as compared to that of typical solvents, such as ethanol (~10 $k_B T$). The fact that $A_{212} = (A_{22}^{1/2} - A_{11}^{1/2})^2 \sim 44$ $k_B T$, for silver in ethanol indicates that Ag nanoparticles experience strong attractions. Substitution of Eq. 25 for Φ_T in Eq. 22 for 2 nm diameter Ag nanoparticles, leads to a stability ratio, $W \approx 1$,

indicating that without electrostatic or steric interactions, primary particles are inherently unstable during early stage growth.

Hence, primary particle stability requires interparticle repulsions. Ag nanoparticles in ethanol experience electrostatic repulsion, Φ_{ELEC}, through the acquisition of surface charge in the presence of ions such as Ag^+, Na^+, NO_3^- .and BH_4^- through dissociation of $AgNO_3$ and $NaBH_4$. To this end, we use the Ohshima potential in Eqs. 26 and 27 for particles of high curvature ($\kappa D < 10$) to model the electrostatic repulsion between nuclei,[36,47]

$$\Phi_{ELEC} = 4\pi\varepsilon r^2 Y^2 \left(\frac{k_B T}{e}\right)^2 \frac{\exp(-\kappa d)}{d+D} \tag{26}$$

$$Y = \frac{8\tanh\left(e\psi_0 / 4k_B T\right)}{1+\left[1-\dfrac{\kappa D+1}{\left(\dfrac{\kappa D}{2}+1\right)^2}\tanh^2\left(e\psi_0 / 4k_B T\right)\right]^{1/2}} \tag{27}$$

where e is the electronic charge. Predictions from this potential depend on the size and surface charge, ψ_0, of the particles. One can use electrokinetic measurements to measure ψ_0, but we obtain it from measurements in previous studies as $\psi_0 = -33$ mV.[43] Moreover, Eqs. 26 and 27 depend on the inverse Debye length, κ, whose inversion captures the thickness of the electrical double layer (EDL) around the particles. The EDL derives from the uneven distribution of ions around a charged surface, defining the extent of repulsion from the nanoparticles. The EDL thickness is sensitive to the solution ionic strength, I, through

$$\kappa = \left[\frac{1000e^2 N_A (2I)}{\varepsilon k_B T} \right]^{1/2}$$

(28)

where $I = (1/2)\sum c_i z_i^2$, ε the dielectric constant of the medium, N_A the Avogadro number, and z_i the ion valence. Overall, increasing ionic strength, I, causes the repulsive electrostatic interaction, Φ_{ELEC}, to decrease, corresponding to a drop in the EDL thickness though κ^{-1} Hence, adding more $AgNO_3$ and/or $NaBH_4$ reduces electrostatic repulsion.

The adsorption of a dodecanethiol brush results in the steric repulsion between interacting Ag nanoparticles. In the model of Vincent and coworkers, they subdivide the steric potential, Φ_{STERIC}, into osmotic and elastic contributions to characterize respectively, brush-solvent interactions and brush compression.[46] The osmotic portion occurs from the energy required for solvent expulsion from the brush upon ligand interpenetration which depends on the solvent molar volume (υ_{solv}), Flory parameter (χ), brush thickness (l), and ligand volume fraction (ϕ) as shown in Eq. 29.[27]

$$\Phi_{OSMOTIC} = \begin{cases} \frac{2\pi D k_B T}{\upsilon_{solv}} \phi^2 \left(\frac{1}{2} - \chi \right) \left(l - \frac{h}{2} \right)^2 & l < h < 2 \\ \frac{2\pi D k_B T}{\upsilon_{solv}} \phi^2 \left(\frac{1}{2} - \chi \right) \left[l^2 \left(\frac{h}{2l} - \frac{1}{4} - \ln\left(\frac{h}{l} \right) \right) \right] & h < l \end{cases}$$

(29)

The brush thickness, l, in Eq. 29 determines the extent over which steric interactions occur, with longer ligands causing the potential to be felt over larger distances, conferring increased stability via the dimensionless separation distance, $h=l/d$. The molecular structure of dodecanthiol was used to estimate the brush thickness by assuming each CH_2 repeat unit was 0.2 nm, yielding l=2.4 nm. The ligand volume fraction, ϕ, relates to the packing of the brush in the 3-D monolayer. Hence, ϕ depends on the ligand surface

coverage, or graft density and ligand brush thickness, *l*. The parameter ϕ can be determined experimentally through elemental and thermal gravimetric analyses;[5,49,50] however, in our calculations we set $\phi=1$ for high surface coverage (e.g., 100%). The final parameter in Eq. 29 is the Flory parameter, χ, which quantifies the mixing energy between ligand and solvent, determines whether the osmotic potential is attractive or repulsive based on the miscibility of the solvent/ligand pair. For our analysis ethanol and the CH_2 repeat units of dodecanthiol were considered miscible, leading to $\chi= 0.4$, for a good solvent.[29]

The second component of Φ_{STERIC} is its elastic contribution due to brush contact with a nanoparticle core, resulting in a repulsive, spring-like interaction in Eq 30.[37]

$$\Phi_{ELASTIC} = \frac{\pi D k_B T l^2 \phi \rho}{\left(M_W\right)^2} \left\{ \frac{d}{l} \ln\left[\frac{d}{l}\left(\frac{3-d/l}{2}\right)^2 \right] - 6\ln\left(\frac{3-d/l}{2}\right) + 3\left(1-\frac{d}{l}\right) \right\} \quad d < l \quad \textbf{(30)}$$

The entire term appearing in braces in Eq. 30 accounts for the functional dependence of Φ_{STERIC} upon brush compression. Additional parameters in Eq. 30 are the ligand mass density, ρ, and the ligand molecular weight, M_W. This equation is valid for $d < l$, when ligands on a nanoparticle contact another nanoparticle core.

Table 1 includes the values of the parameters and constants for use in Eqs. 25-30. In the next subsection, we analyze the calculations of the total or net interaction potential in Eqs. 24-30 to gain insight and develop hypothesis for controlling the early-stage growth of functionalized Ag nanoparticles.

Table 1. Parameters for Eq. 25-30 used to produce Figure 3, 4, and 5.

Parameters for Calculation of Net Interaction Potential - Φ_T	
A_{11}, Hamaker constant – ethanol[34]	4.2E-20 J
A_{22}, Hamaker constant – silver[34]	3.98E-19 J
D, nanoparticle diameter[16]	2 nm
T, temperature	298 K
ε, dielectric constant - ethanol	24.3
I, ionic strength	40 mM
Ψ_δ, surface charge – silver nanoparticle[48]	-33 mV
υ_{solv}, molar volume - ethanol	58.4 cm^3/mol
χ, Flory parameter – DDT/ethanol	0.4
Φ, ligand volume fraction	1
l, brush thickness	2.4 nm

2.5 Analysis of the net interaction potential and its implications on early stage growth

In this section, we calculate the net interaction potential, Φ_T, from Eqs. 24-30 from the parameters and constants in Table 1to elucidate the reaction conditions that control the early-stage growth of the dodecanethiol-functionalized Ag nanoparticles. Since our goal is to achieve colloidal stability at a size close to that of the primary particles, it makes sense to set up our calculations to reflect these conditions. In general,

this means that we model Φ_T based on the relevant constants for the solvent, ethanol. Moreover, we model electrostatic interactions accounting for both the particle surface potential and electrical double layer whose thickness depends up the concentrations of ions from the dissociation of $AgNO_3$ and $NaBH_4$ at concentrations that occur within our experiments. Steric interactions are calculated to quantify the effect of the dodecanethiol brush on stabilizing primary particles with a fixed diameter of $D=2$ nm. To illustrate the interactions at work in the reaction system, the results of the calculations are shown in Figure 3-5 below.
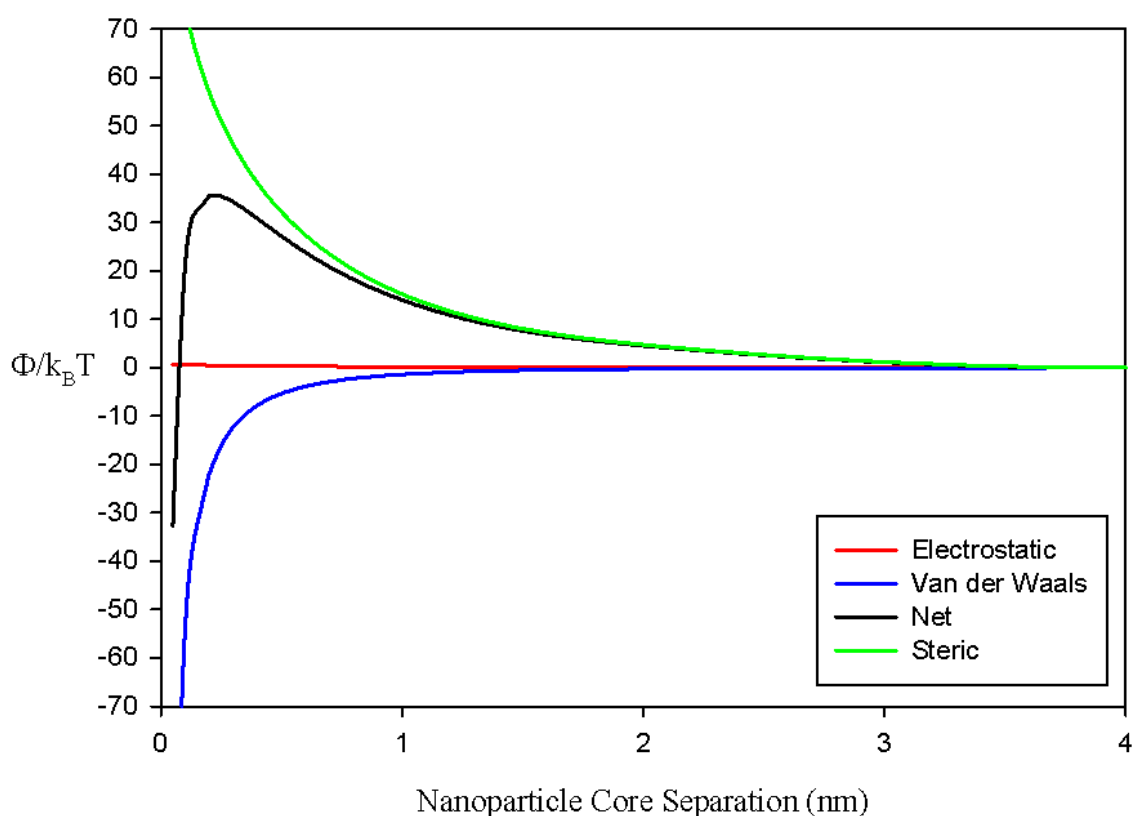
Figure 3. Interparticle interaction potentials plotted as a function of nanoparticle separation. It is clear from comparison of the electrostatic and steric forces that the steric interaction is the dominant repulsive contributor to the net interaction potential.

In Figure 3 we model the effect of monolayer coverage on particle stability where the van der Waals contribution to the net interaction potential Φ_T scaled by $k_B T$ is in blue, the electrostatic interaction in red, the steric interactions in green, and Φ_T in black. The ion concentrations correspond to $[AgNO_3]$=10 mM and $[NaBH_4]$=30 mM, resulting in a ratio, R=$[NaBH_4]/[AgNO_3]$=3, which we use to track the effect of the reducing agent in our experiments. The van der Waals interaction has its characteristic downturn at close particle approach indicative of strong particle attractions. The electrostatic potential, which is influenced by the ion concentration through R, is nearly flat, indicating that electrostatic interactions play a minor role in the stabilization of primary particles as R=3 corresponds to the lowest ionic strength and the largest electrical double layer thickness and electrostatic repulsion in our study. Most importantly, it is apparent in Figure 3 that the steric interaction, which arises as a direct result of dodecanethiol brush adsorption offers the main opposition to van der Waals interaction, resulting in maximum in Φ_T= 35 $k_B T$. Substitution of Φ_T from Figure 3 into Eq. 22 yields a stability ratio, W=10^{13}, which is indicative of *very* stable primary particles. Hence, the production of stable Ag primary particles requires the presence of a densely packed SAM brush. To this end, dodecanethiol functionalization during Ag nanoparticle nucleation and growth requires control over the reaction conditions. We hypothesize that the best opportunity for early stage functionalization is to use low $[AgNO_3]$ (e.g., 10 mM) to slow nucleation and growth permitting the end-on adsorption of dense dodecanethiol brushes. This will lead us to increase the dodecanethiol concentration as tracked by the ratio, S=$[DDT]/[AgNO_3]$, as we hypothesize that elevating $[DDT]$ will increase its mass transfer to the nanoparticle surface, resulting in adsorption and particle stability.

Analysis of Figure 4 further illustrates of the insignificance of electrostatic, electrical double layer repulsion on early stage stability of Ag nanoparticles by varying [NaBH$_4$] to change the R-ratio from R = 3-12. Figure 4 shows Φ_T with contributions from van der Waals, electrostatic, and steric interactions as well as the electrostatic interaction potential. In particular, the inset in Figure 4 shows that the maximum in Φ_T changes by less than 1 k_BT over a four-fold increase in ionic strength from R=3-12 . This lack of influence of R on Φ_T indicates that increasing [NaBH$_4$] in the presence of a dense dodecanethiol brush should have a minimal effect on early stage growth. Hence we hypothesize that one can add an arbitrarily high amount of [NaBH$_4$] (up to its solubility limit in ethanol) and stabilize nanoparticles via steric repulsions, while collapsing the electrostatic double layer in the process.

To discern the effect of ligand surface coverage on steric interactions and Φ_T, the latter was evaluated as a function of ligand coverage varying from 100% for a dense monolayer and reductions in monolayer coverage between 0-75%. The resulting data are displayed in Figure 5, which illustrates the importance of a densely packed SAM on particle stability, where coverages of 50% and below lead to unstable nanoparticles based on the maximum in Φ_T<3 k_BT.[30] In light of this prediction, we hypothesize that it is imperative to have a sufficiently high [DDT] or S ratio, to fully functionalize and stabilize the primary particles.

In the next section we summarize our predictions and state the objectives of this thesis.
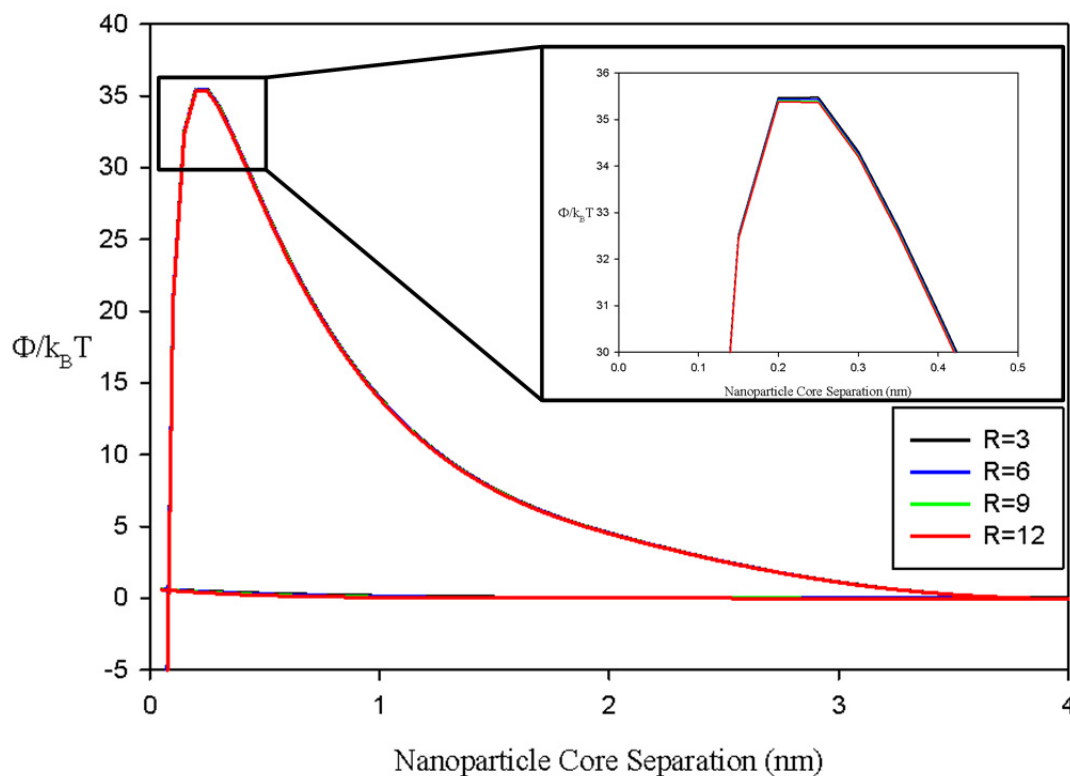
Figure 4. Net and electrostatic potential as a function of reducing agent ratio, $R=[NaBH_4]/[AgNO_3]$ at full monolayer coverage. In the main plot, the lower curve is the electrostatic potential and the upper curve the net interaction potential. The inset shows the maximum in the net interaction potential at 30-36 k_BT. Increasing R does not appreciably lower the net interaction potential, indicating the minimal importance of electrostatic interactions.
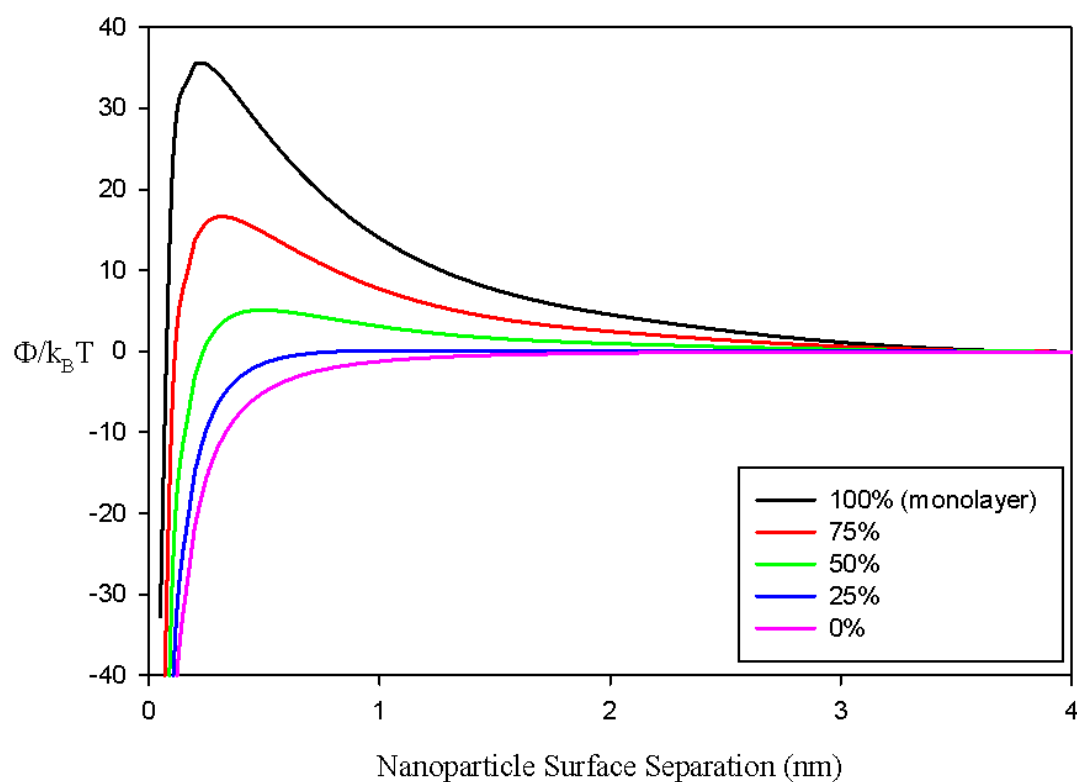
Figure 5. Plot of the net interaction potential as a function of ligand coverage. Decreasing the surface coverage reduces the steric potential, resulting in a large decrease of the net interaction potential, which decreases particle stability.

2.6 Summary of Analyses and Statement of Objectives

From the analyses in the previous sections, we arrive at the following suppositions:

- Slowing the primary particle growth rate depends upon lowering [AgNO$_3$] to a low concentration to slow nucleation and reduce the number of nuclei to enable the adsorption of a dense, end-tethered dodecanethiol brush during early stage growth.

- Early stage particle stability requires the adsorption of dense dodecanethiol brushes whose adsorption can be optimized by elevating [DDT] to increase its mass transfer to the surface of the primary particles.

- Electrostatic forces do not play a major role in the stability of dodecanethiol functionalized Ag nanoparticles at the early stages of growth, which means that [NaBH$_4$] can be increased up to its solubility limit.

- Lower dodecanethiol surface coverages can lead to primary particle instability and aggregation, indicating the importance of sufficient [DDT] to form a dense brush layer on the primary particles.

Hence, our objectives in achieving a scalable, one-phase, one-step, room temperature synthesis to produce uniform, spherical, dodecanthiol-functionalized Ag nanoparticles are as follows:

1. To determine the effect of R=[NaBH$_4$]/[AgNO$_3$] and S=[DDT]/[AgNO$_3$] on the size and uniformity of Ag nanoparticles. We expect these factors to

primarily influence adsorption of a dense dodecanethiol brush layer, rate of Ag^0 appearance via reduction, and thickness of the electrical double layer.

2. To elucidate the effect of high [NaBH$_4$], through R, on colloidal stability of Ag nanoparticles. We expect high R to result in collapse of the electrical double layer, minimizing electrostatic interactions.

The resulting nanoparticles were characterized with TEM to determine the particle size and uniformity, as well as UV-VIS spectrophotometry to confirm the presence of the surface plasmon for DDT-functionalized Ag nanoparticles around $\lambda \approx 450$ nm. Additionally, at high [NaBH$_4$], or high R=72-108, we detected didodecyl disulfide which we postulate forms through a silver-mediated oxidation of dodecanthiol. The use of dodecyl disulfide in nanoparticle synthesis is expected to behave similarly to dodecanthiol with respect to the formation of dense ligand monolayers, as indicated by the studies of Whitesides and coworkers.[51]

In the next section, Experimental Methodology, we describe in depth the reaction scheme used to synthesize the DDT-functionalized Ag nanoparticles as well as the methods of their characterization.

3.   Experimental Methodology

3.1 Materials for Silver Nanoparticle Synthesis

ACS reagent grade absolute ethanol ($\geq$99.5% purity) and toluene were purchased from Fisher Scientific and used as solvents for the nanoparticle synthesis. Dichloromethane ($\geq$99.9% purity) and potassium bicarbonate ($KHCO_3$, USP/FCC) were purchased from Fisher Scientific for use in the synthesis of didodecyl disulfide.   Silver nitrate ($AgNO_3$, ACS reagent grade, $\geq$99% purity), sodium borohydride ($NaBH_4$, $\geq$96% purity), 1-dodecanethiol (DDT, $\geq$98% purity), and bromine (Br_2, ACS reagent grade, $\geq$99.5% purity) were purchased and used as received from Sigma-Aldrich.

3.2 Synthesis of 1-dodecanethiol Functionalized Silver Nanoparticles

On the basis of work from Zukoski et al.,[15] we developed a straightforward, scalable method to synthesize alkanethiol-stabilized silver nanoparticles in ethanol. The method equates to a one-pot, one-phase synthesis that involves mixing the reactants from two separate vials in which the first vial contains the metal salt precursor ($AgNO_3$) dissolved in ethanol, while the second vial contains the alkanethiol surfactant (1-dodecanethiol - DDT), reducing agent ($NaBH_4$), and solvent. We illustrate the mixing protocol in Figure 6. We found that adding DDT to the first vial with $AgNO_3$ lead to the formation of insoluble silver thiolates, a yellowish species that interferes with consistent nanoparticle formation.[46]
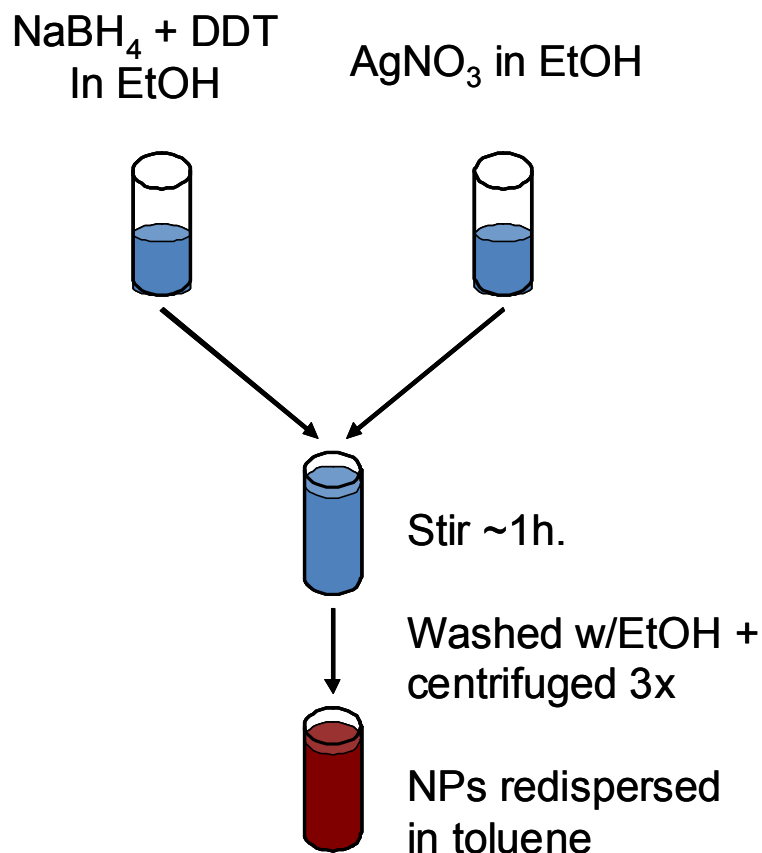
Figure 6. A schematic of the mixing protocol for the synthesis of DDT-functional Ag nanoparticles. NaBH$_4$ and dodecanethiol are dissolved in ethanol (EtOH) in one vial, and AgNO$_3$ in ethanol in the second vial. The two vials are combined, stirred ~1 hour, centrifuged and washed three times with ethanol before redispersion in toluene.

The method in Figure 6 presents a starting point to control the synthesis of alkanethiol-stabilized nanoparticles in bulk solutions by controlling nucleation which depends on the metal salt and reducing agent concentrations, and growth which depends on the concentrations of the alkanethiol and ions in solution.[15] We contend that a mechanistic understanding of how reactant concentrations impact nucleation and growth enables the synthesis of monodisperse nanoparticles, precluding the use of more ad-hoc, less scalable methods such as the dropwise addition of metal precursors and reducing agents in an effort to control nanoparticle formation.[7]

The mechanistic studies of Zukoski and Polte indicate that a particle growth follows a rapid burst of nucleation where primary nuclei are inherently unstable and aggregate through attractive van der Waals interactions until the particles reach a final size that depends upon the magnitude of the electrostatic interactions.[15,16] On the basis of DLVO theory, the magnitude of the electrostatic interaction depends on the particle surface charge, solution ion concentration, and ion valence, the last of which has a value of unity for symmetric 1:1 salts such as $AgNO_3$ and $NaBH_4$. Moreover, Zukoski and Polte both exploited the effects of steric stabilizing agents (e.g., polyvinyl alcohol and polyvinylpyrrolidone) to halt nanoparticle growth by providing a steric barrier against aggregation.[15,16] This result represents the starting point of our work as we hypothesize that we can halt particle growth close to the size of the primary nuclei through the end-on adsorption of 1-dodecanethiol in ethanol.

Hence, a matrix of 16 samples was formulated as listed in Table 2 using the following general procedure. First, two stock solutions in ethanol were produced: 0.02 M $AgNO_3$ and 0.24 M $NaBH_4$. The $NaBH_4$ solution was serially diluted to appropriate concentrations and 9 mL transferred to each of 16, 20 mL vials. The final concentrations of the $NaBH_4$ solutions were selected such that upon mixing, the $[NaBH_4]/[AgNO_3]$ ratio, denoted R, would be 3, 6, 9, or 12. 1-dodecanethiol was added to each of the vials containing the $NaBH_4$ solution at $[DDT]/[AgNO_3]$ ratios, denoted S, of 1, 3, 6, and 12, for a total of 16 samples. 9 mL of the $[AgNO_3]$ stock solution was pipetted into a clean vial and added in one continuous pour to one of the sixteen vials. This step was repeated for each of the remaining 15 vials. Upon addition of the $[AgNO_3]$, the combined solution immediately turned to a dark brown color before gradually darkening to pitch black. The

vials with the combined AgNO₃, NaBH₄, and dodecanethiol solution were stirred for 1 hour at room temperature.

Table 2. The matrix of 16 samples used to investigate the influence of $NaBH_4$ and dodecanethiol on the final nanoparticle product. Expanding on the notation of Zukoski,[15] we find it convenient to encapsulate the concentrations in the ratios $R=[NaBH_4]/[AgNO_3]$ and $S=[DDT]/[AgNO_3]$.

[Ag]=10 mM in 18 mL ethanol; all concentrations in mM			S			
			1	3	6	12
R	3	$[NaBH_4]$	30	30	30	30
		[DDT]	10	30	60	120
	6	$[NaBH_4]$	60	60	60	60
		[DDT]	10	30	60	120
	9	$[NaBH_4]$	90	90	90	90
		[DDT]	10	30	60	120
	12	$[NaBH_4]$	120	120	120	120
		[DDT]	10	30	60	120

3.3 Synthesis of 1-dodecanethiol Functionalized Silver Nanoparticles at High Salt

Concentrations

Particles were synthesized with high NaBH₄ values, $R=72$ and $R=108$, to elucidate the effect of ion concentration on nanoparticle stability. For these trials, 18 mL of a 0.1 M AgNO₃ in ethanol solution was made and diluted to 2.25 mM through two dilutions. In the first dilution 2.7 mL of the AgNO₃ solution was diluted to 18 mL with fresh ethanol. In the second dilution 2.7 mL from the first dilution was diluted it to 18 mL with fresh ethanol. A 69.4 mM NaBH₄ in ethanol stock solution was then made by dissolving 0.2625 g NaBH₄ in 100 mL ethanol. In one 20 mL borosilicate glass vial containing 14 mL of the stock NaBH₄ solution, 25.7 μL of DDT was added, giving final values of $R=108$, $S=12$. In another 20 mL borosilicate glass vial, 9.34 mL of the stock NaBH₄

solution was diluted with 4.66 mL ethanol and 25.7 μL dodecanethiol was added, giving

final values of R=72, S=12. Two 4 mL volumes of the diluted AgNO$_3$ solution were

pipetted into two clean borosilicate vials and added in one continuous pour to each of the

NaBH$_4$ solution vials to bring the final silver concentration to 0.5 mM. Upon addition of

the AgNO$_3$, the combined solution slowly turned dark yellow color before gradually

turning a yellowish-brown. The vials with the combined AgNO$_3$, NaBH$_4$, and

dodecanthiol solution were stirred for 1 hour at room temperature.

3.4 Purification of Silver Nanoparticles

To purify the nanoparticles, solutions were poured into fluorinated centrifuge

tubes and centrifuged at 8000 RPM for 20 minutes. The supernatant was then decanted

and the centrifuge tubes were refilled with fresh ethanol and sonicated to redisperse the

Ag nanoparticles. This cycle was repeated three times. Subsequently, 20 mL of toluene

was added to nanoparticles and the suspensions were sonicated to redisperse the

nanoparticles before transfer to final storage in borosilicate vials. The nanoparticle

suspensions were characterized using ultraviolet-visible (UV-VIS) spectroscopy and

transmission electron microscopy (TEM).

3.5 Synthesis of Didodecyl Disulfide and Didodecyl Disulfide Functionalized Silver
    Nanoparticles

We consistently observed an absorption peak at a wavelength of λ≈300 nm in the

UV-VIS spectra for nanoparticles synthesized at high [NaBH$_4$] with R=72 and 108. Our

prevailing hypothesis regarding this peak was to attribute it to the formation of didodecyl

disulfide. To test our hypothesis, we synthesized it by adapting the method of Abbot and Hendrick;[53] we then took its UV spectrum, and compared it to the 300 nm peak in the high salt samples. To synthesize didodecyl disulfide, 20 mmols (4.79 mL) dodecanethiol was dissolved in 150 mL dichloromethane in a round bottom flask. To this was added 20 mL of a 10% (by volume) potassium bicarbonate solution in water. 0.5 mL bromine (~10 mmols) was added to the mixture under stirring. The color of the bromine quickly disappeared upon addition. The organic phase was separated and set aside. The aqueous phase was washed with 50 mL dichloromethane before again separating the organic phase. The organic phases were combined and dried over magnesium sulfate. The mixture was filtered to remove the magnesium sulfate and then dried under vacuum to recover the crude product. Characterization of the oily, off-white solid was performed using UV-VIS spectroscopy.

3.6 Ultraviolet-Visible (UV-VIS) Spectroscopy

A SpectraMax Plus 384 Absorbance Microplate Reader ultraviolet-visible spectrophotometer was used to characterize the absorbance of nanoparticle solutions. Nanoparticle solutions were pipetted into quartz cuvettes and scanned wavelengths between $\lambda=190\text{-}800$ nm in 10 nm increments, collecting absorbance data at each wavelength. For some particle solutions, spectra were taken with 1 nm wavelength increments to collect more precise measurements of the absorbance. To ensure accurate measurement of absorbance, nanoparticle solutions were diluted to ensure measured absorbance was kept below a value of 1. For the 16 standard experimental setups (section 1.2 above) nanoparticle solutions were diluted down by mixing 0.5 mL of solution with

2.5 mL fresh toluene. For the nanoparticle solutions produced using increased salt concentration (Section 1.3), no dilution was necessary. For the absorbance measurement of didodecyl disulfide, the product was dissolved in toluene and the spectrum taken.

3.7 *Transmission Electron Microscopy*

A JEOL 2000FX Transmission Electron Microscope (TEM) at an accelerating voltage of 200 kV was used to quantify the size and the size distribution of the nanoparticles. Sample preparation of the TEM grids was done by a drop mounting method. A carbon film on 400 mesh copper grid was held within self-closing tweezers; a pipette was used to place a drop of nanoparticle solution in toluene onto the grid. A small piece of filter paper is used to wick any extra solvent away and the grid is left to dry for at least one hour. Determination of nanoparticle size was performed using automated routines built into the freely available ImageJ software developed by the National Institutes of Health.

4. Results and Discussion

Based on the analysis of the theories of nucleation and early-stage growth, we sought to determine the effect of varying the reducing agent concentration (via R=[NaBH$_4$]/[AgNO$_3$]) and the dodecanethiol concentration (via S=[DDT]/[AgNO$_3$]) on the formation of Ag nanoparticless while holding the metal salt concentration constant at [AgNO$_3$]=10mM. We hypothesize that the manipulation of R and S facilitates control over the early stages of nanoparticle nucleation and growth, leading the production of spherical, dodecanethiol-functionalized Ag nanoparticles. Hence, a matrix of 16 Ag nanoparticle samples were synthesized over a sweeping parameter space from R=3-12 and S=1-12. The average particle size and polydispersity of each sample was characterized with TEM to judge the success of the synthetic conditions in achieving particle uniformity. UV-VIS spectroscopy was used as a complementary technique to quantify the plasmon resonance of the DDT-functionalized Ag nanoparticles which absorb around $\lambda \approx 450$ nm.[54]

Moreover, to extend our examination of R and S to a comparison of the importance of electrostatic and steric forces on nanoparticle stabilization during early-stage growth, two samples of Ag nanoparticles were synthesized with high [NaBH$_4$] resulting in R=72 and 108. As the theoretical calculations of the interaction potentials in Figure 3 illustrate that primary particles with D=2 nm are inherently unstable without steric interactions, we anticipate that while the extreme ion levels at 0.72-1.08 M would collapse the electrostatic double-layer, this collapse would have minimal impact on particle stability. Hence, the stability of primary particles in solutions of high ionic strength would highlight the importance of the end-on adsorption of dodecanethiol. This

treatment will permit us to test our hypothesis that the dodecanethiol brush layer is the primary contributor to nanoparticle stability during early stage growth.

During the analysis of the UV-VIS spectra of samples with high R=72-108, we detected didodecyl disulfide, which forms through the two electron oxidation of two molecules of dodecanethiol.[55] As we do not detect didodecyl disulfide in the absence of Ag nanoparticles, we suspect the two-electron transfer process is catalyzed by elemental silver. We confirmed the presence of didodecyl disulfide by synthesizing it and then using. UV spectroscopy to determine the absorption wavelength which was compared to spectra of the DDT-functionalized Ag nanoparticle samples with a potential disulfide peak.[53] Further, to investigate the effect of didodecyl disulfide on Ag nanoparticle formation, we replaced dodecanethiol with didodecyl disulfide as a capping agent in our synthetic protocol, and characterized the resulting nanoparticles with TEM.

4.1 Silver Nanoparticle Synthesis

In general, 4-5 TEM images were taken of each of the 16 samples synthesized in our [AgNO$_3$]=10 mM, R=3-12, S=1-12 parameter space. The image analysis software, ImageJ, was used to calculate of the number-average particle diameter as well as the standard deviation of the particle size, resulting in the calculation of the relative standard deviation, i.e., the ratio of the standard deviation and average size from at least 200 nanoparticles. The relative standard deviation is also referred to as the polydispersity. Representative images for each sample, from which the average size and polydispersity were calculated, appear in Figure 7.

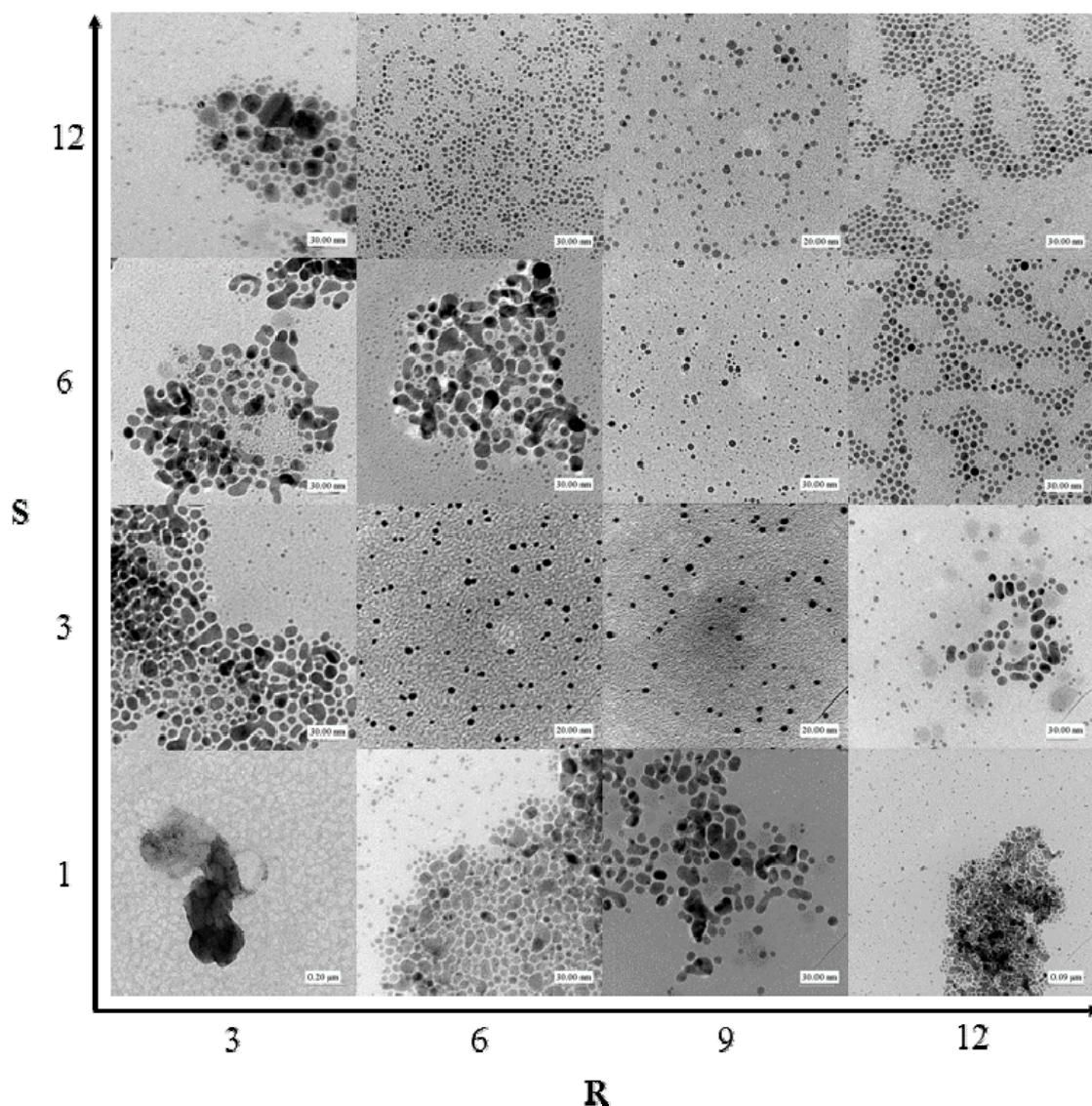**Figure 7.** Representative TEM images of each sample in the parameter space R=3-12, S=1-12 with [AgNO$_3$]=10mM. Sizing of nanoparticles and calculation of the polydispersity were performed through the image analysis software ImageJ. In general, at least 200 nanoparticles were sized to calculate the average diameter and standard deviation. The diameter and deviation for each sample is tabulated in Table 3.

From direct observation of the images in Figure 7, it is clear that nanoparticles synthesized at low R or S, respectively, the leftmost column and the bottommost row, are very polydisperse. In fact, syntheses under these conditions result in a bimodal particle size distribution as illustrated by a representative TEM at $R=6:S=1$ in Figure 8 which shows smaller particles of $D=3$ nm with larger particles of $D=10$-30 nm.

The wide distribution in particle size apparent in Figure 8 is consistent with the trends in Figure 5 as well as our expectations for the effect of low [DDT], which we anticipate will lead to sub-monolayer ligand coverage, resulting in nanoparticle aggregation. The effect of insufficient reducing agent at low R on nanoparticle stability was not specifically predicted in calculations in Figures 3-5; however, particle instability at low R is reasonable as Zukoski and coworkers report similar findings.[15]

It is also possible to observe another regime in Figure 7 in which uniform, spherical DDT functionalized Ag nanoparticles were produced. This region exists roughly from $R=6$-12 and $S=3$-12, with the exception of the $R=6:S=6$ and $R=12:S=3$ samples, which we regard as anomalous. The average nanoparticle diameter in the region of nanoparticle uniformity ranges from 3.5-4.7 nm, with polydispersity decreasing with increases in R and S (i.e. moving to the upper-right in Figure 7). Based on the standard deviation in particle size in Table 3, a significant population of stable nanoparticles exists at or near the primary particle diameter of $D\approx2$nm. An image that effectively illustrates Ag nanoparticle uniformity is shown in Figure 8.
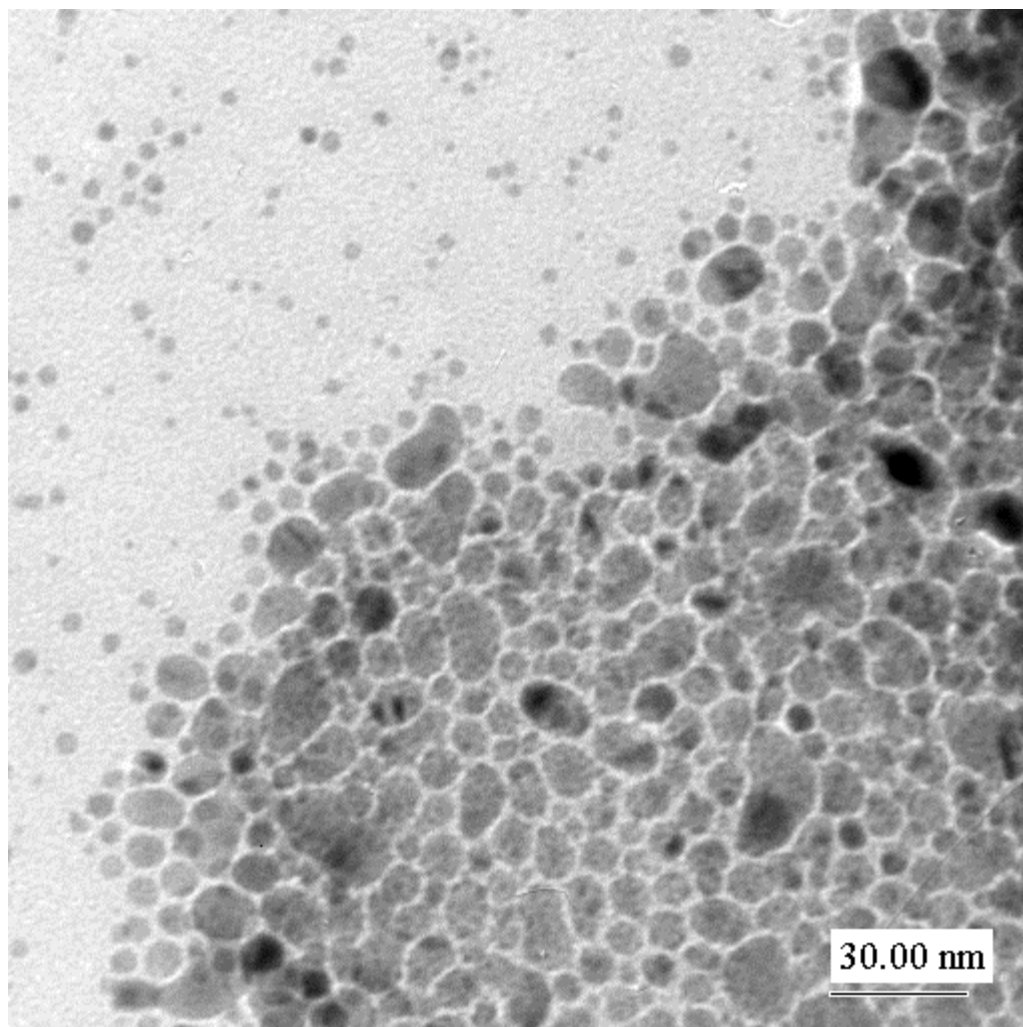
Figure 8. TEM image of the *R*=6:*S*=1 sample. The nanoparticles in this image are divided into two distinct size regimes, with the right side being mostly irregular, aggregates and the upper left being spherical nanoparticles. This gives rise to a bimodal size distribution as reflected in the average diameter, *D*=5.6±20.0 nm. As the particles were synthesized with a dodecanthiol ratio, *S*=1, these results suggest that nanoparticles lack a densely monolayer, permitting aggregation.
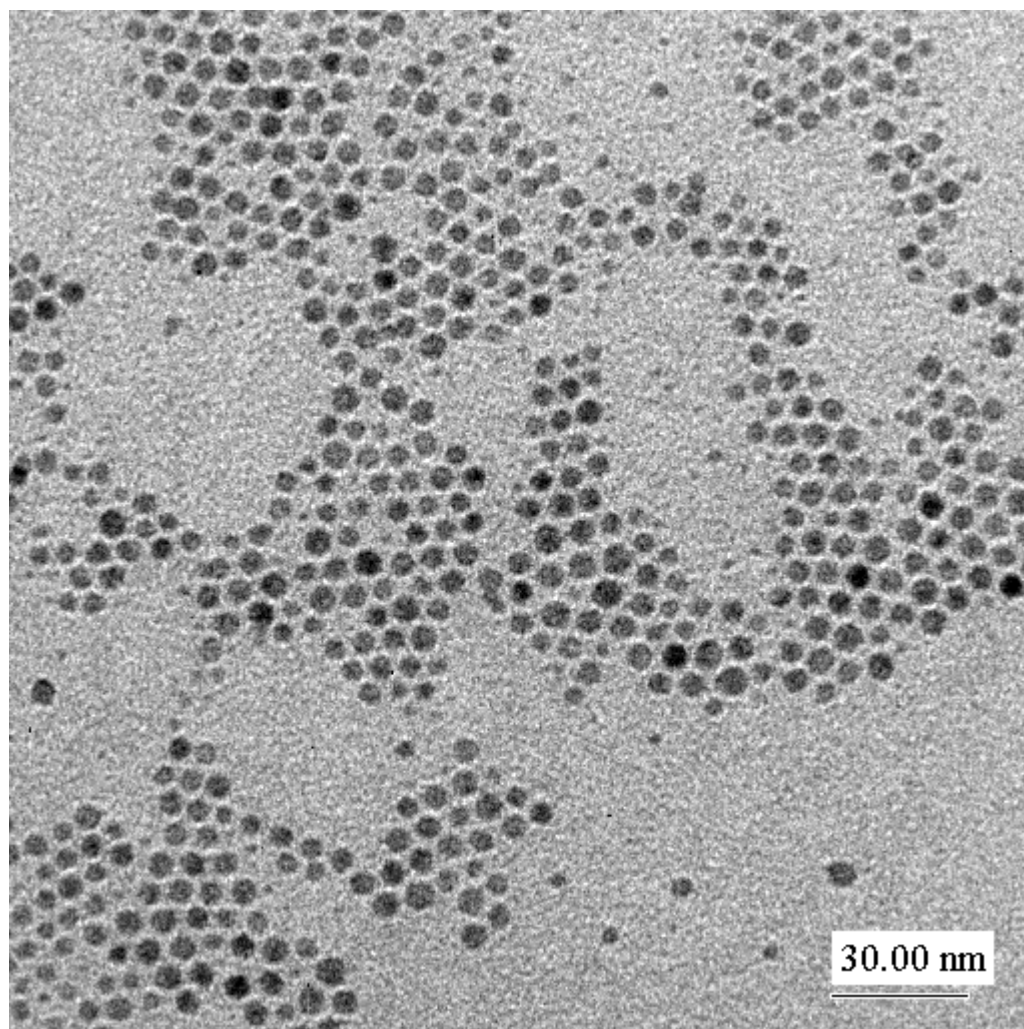
Figure 9. TEM image of the *R*=12:*S*=12 Ag nanoparticle sample. The nanoparticles are uniform and spherical with an average diameter of *D*=4.7±1.6 nm. The high uniformity coupled with the small particle size lends support to our hypothesis that steric repulsion from the adsorption of dodecanethiol stabilizes these particles at early reaction times.

Further exposition of the data extracted from the samples constituting Figure 7 serve to make the regions of particle uniformity and non-uniformity more clear. Prior to displaying this data, we should point out that the highly bimodal particle size distributions at low R or S lead to standard deviations that exceed the mean diameter. One obviously cannot obtain negative particle sizes; hence, we report the standard deviation on the 95% confidence interval as an indicator of polydispersity. Without further exposition, the particles sizes from the samples in Figure 7 are shown in tabular form in Table 3.

Table 3. Average nanoparticle diameter with standard deviation calculated on a 95% confidence interval (CI). The data were extracted from TEM images of the 16 samples illustrated Figure 1. Data marked with an asterisk is characteristic of a bimodal particle distribution, which gives rise to a very large 95% CI.

[AgNO$_3$]=10 mM in all samples		R=[NaBH$_4$]/AgNO$_3$]			
		3	6	9	12
S=[DDT]/[AgNO$_3$]	12	2.0±2.4*	3.7±2.1	3.5±1.8	4.7±1.6
	6	7.8±18.5*	6.3±18.3*	3.5±2.8	4.0±1.4
	3	5.6±19.5*	3.7±1.7	4.0±1.6	4.9±6.6*
	1	3.4±9.6*	5.6±20.0*	10.9±15.1*	4.9±29.1*
* indicates a bimodal distribution of particle diameters					

The data in Table 3 serve to reinforce the trends in nanoparticle uniformity as a function of R and S. Further illustrations of these trends are observed in the contour plots of diameter and the relative standard deviation of the diameter – the latter a measure of polydispersity. These quantities are displayed as functions of reducing agent and dodecanethiol ratios R and S in Figures 10 and 11.
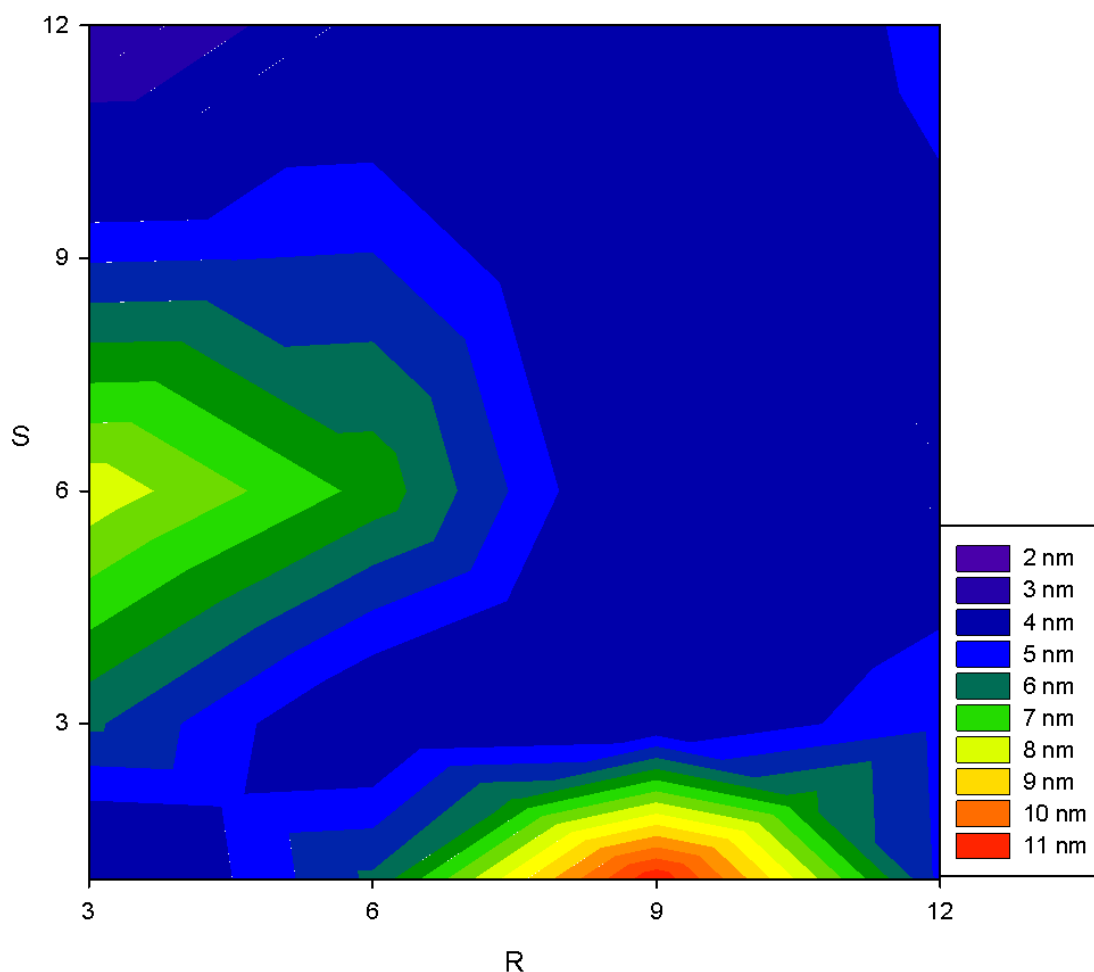
Figure 10. Contour plot of the average nanoparticle diameter, *D*, as a function of reducing agent and dodecanthiol ratios, *R* and *S*. Regions with *D*>5nm are undesirable for our purposes; however, a *D*≤5nm is not a sole indicator of a good synthesis. Hence, the analysis of this plot should be taken in conjunction with that in Figure 11 which shows the relative standard deviation (RSD) of the nanoparticle diameter. A region of colloidal stability has both a low diameter and a low RSD.
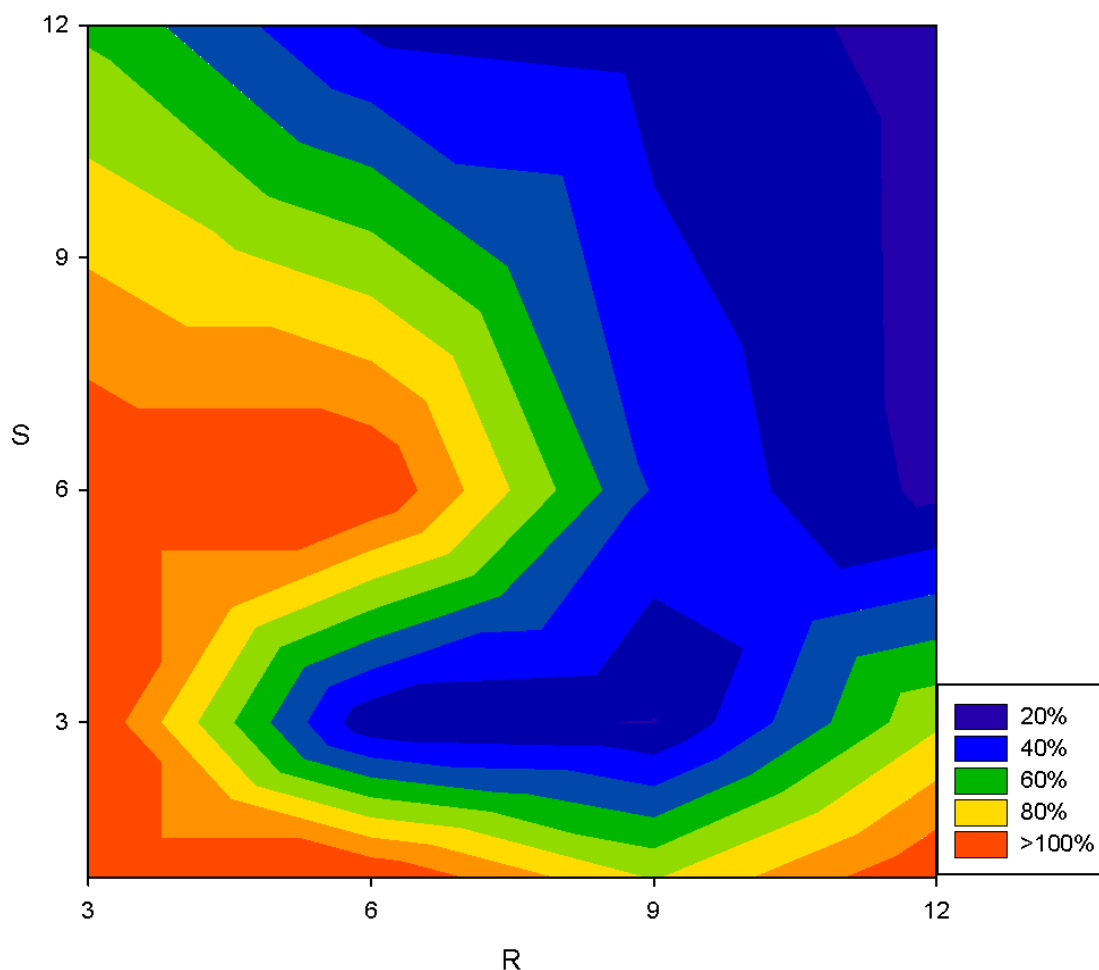
Figure 11. Plot of the relative standard deviation (RSD) of nanoparticle diameter as a function of reducing agent and dodecanethiol ratios, *R* and *S*. The regions with the best (lowest) RSD are high *R*, high *S* samples. At low values of either *R* or *S*, it is clear that the nucleation and growth process are not effectively controlled, leading to aggregate formation and higher RSD. These results are in line with our expectations of how the reaction system should behave. Low *S* appears to result in sub-monolayer ligand coverage, leading to particle aggregation. Low *R* is reported to result in the formation of aggregates, as per the work of Zukoski and coworkers.[15]

From Figure 10 and 11, it is apparent that increasing the reducing agent and dodecanethiol ratios, *R* and *S*, respectively, improves nanoparticle uniformity, as expressed through a decrease in the relative standard deviation (RSD). Once again, this result in line with our hypotheses based on Figure 3 where a higher dodecanethiol ratio, *S*, promotes adsorption and stability of the primary particles via steric repulsion. Moreover, we find that a higher reducing agent ratio, *R*, decreases the polydispersity as shown in Figure 11.

To further characterize the samples, UV-VIS spectra were taken to detect the characteristic surface plasmon resonance band (SPR) for the Ag nanoparticles at a wavelength of $\lambda_{spr} \approx 450$ nm. In general, the absorbance wavelength becomes independent of size for *D*<15nm as the particles become much smaller than the instrumental λ[16,54] In Figure 12 we show only the UV spectra for samples in the region of nanoparticle uniformity which essentially conform to a size-independent λ_{spr}. In this figure we exclude the aggregated samples from row *R*=3 or column *S*=1 in Figure 7, as these spectra either "red-shift," i.e., shift to higher λ due to light scattering from larger suspended particles, or resemble the spectra in Figure 12 denoting only the presence of small Ag nanoparticles in solution. We anticipate that the aggregated suspensions will "red-shift"; thus, the lack of "red-shifting" is in conflict with the bimodal size distribution displayed in the TEM images in Figures 7 and 8, indicating that the larger aggregates settled out of suspension before data collection; with that in mind, the absorbance band at $\lambda_{spr} \approx 450$nm in Figure 12 confirms the synthesis of small Ag nanoparticles within the region of particle uniformity at *R*≥6-12 and *S*≥3-12 in Figure 7.
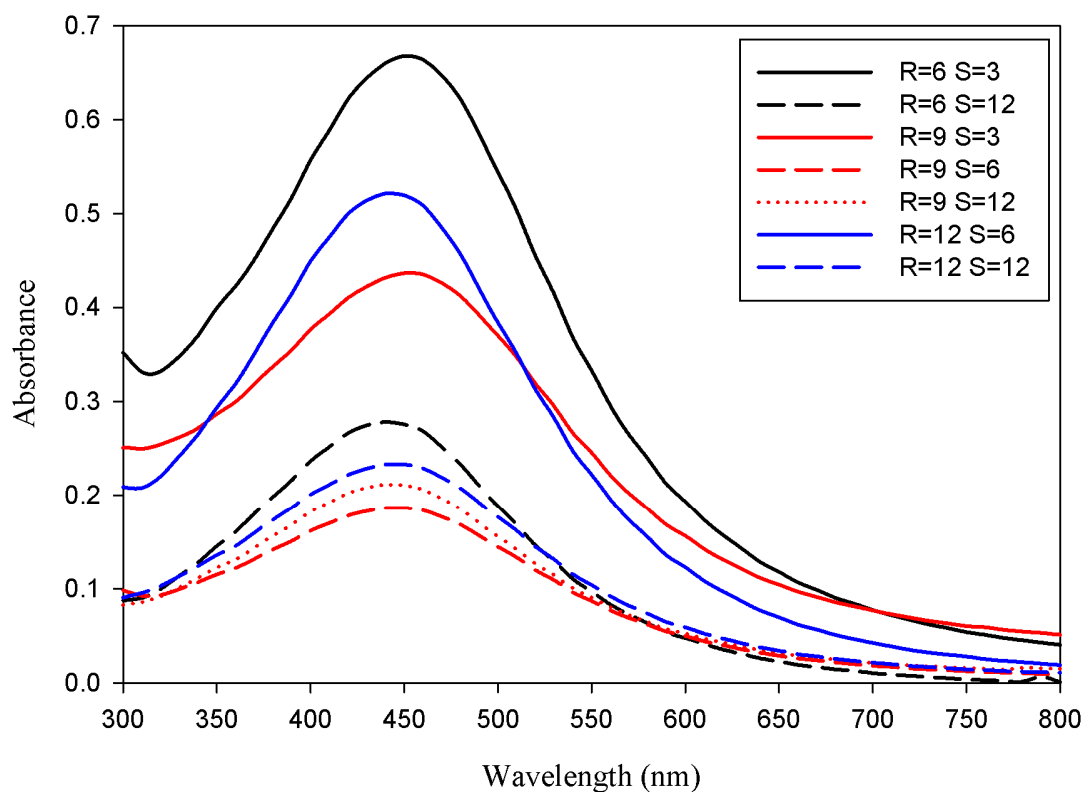
Figure 12. UV-VIS spectra of DDT-functionalized Ag nanoparticles in toluene. Curve color is consistent within a given *R* value. The primary feature is the surface plasmon absorption band at $\lambda_{abs} \approx 450$nm which serves to confirm the presence of Ag nanoparticles.

To summarize the findings from this section, the TEM and UV-VIS spectroscopy results support our hypotheses that we can produce uniform, spherical DDT-functionalized Ag nanoparticles with sizes close to that of the primary particle by manipulation of the parameters *R* and *S* in a straightforward, one-phase, synthetic method. In the next section we extend the synthesis to high ionic strength solutions.

4.2 Synthesis of DDT-functionalized Nanoparticles at High Ionic Strengths

Based on the net interaction potential calculations in Figure 5 of Chapter 2, we hypothesize that it would be possible to stabilize Ag nanoparticles at a size close to the primary particle diameter of 2 nm through steric interactions at high reducing agent concentrations. To test this hypothesis, we extended our technique to synthesize nanoparticles at extreme values for *R*. If the magnitude of the steric interaction is sufficient, we then expect to produce small, uniform nanoparticles. Hence, two samples were made, one with a reducing agent ratio of *R*=72 and the other with *R*=108. [AgNO$_3$] and the dodecanethiol ratio *S* were held constant at 10 mM and 12, respectively. Both samples were characterized via TEM and ImageJ analysis as well as UV-VIS spectrophotometry with the results displayed in Figures 13 and 14.

From the TEM images and the UV-VIS spectra in Figures 13 and 14, it is clear that small, uniform, spherical nanoparticles form in high ionic strength solutions as represented by *R*=72-108 where electrical double layer collapsed is expected. These findings support our hypothesis that the adsorption of dodecanethiol stabilizes the primary particles in the absence of electrostatic repulsion at high ionic strength. Subsequently, we turn our attention to the absorbance peak at $\lambda_{abs}\approx300$ nm in Figures 13 and 14 which we postulate is due to the *in-situ* formation of didodecyl disulfide. The next section deals with our efforts to investigate this postulate and related results.
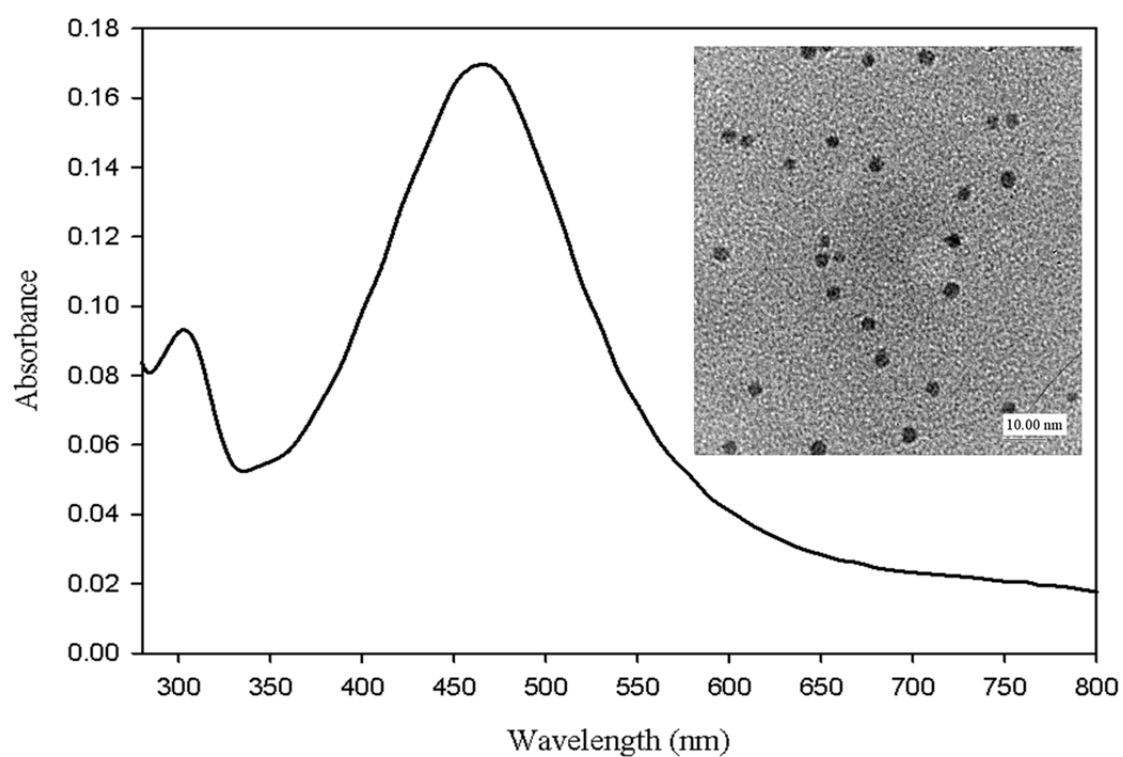
Figure 13. UV-VIS spectrum of R=72 S=12 Ag nanoparticles with TEM inset. The absorbance peak at $\lambda_{spr} \approx 450$ nm signifies the presence of small Ag nanoparticles in toluene. The peak at λ_{abs}= 300 nm is attributed to the *in-situ* formation of didodecyl disulfide. The TEM image confirms the presence of uniform nanoparticles with D=3.5±0.8 nm.
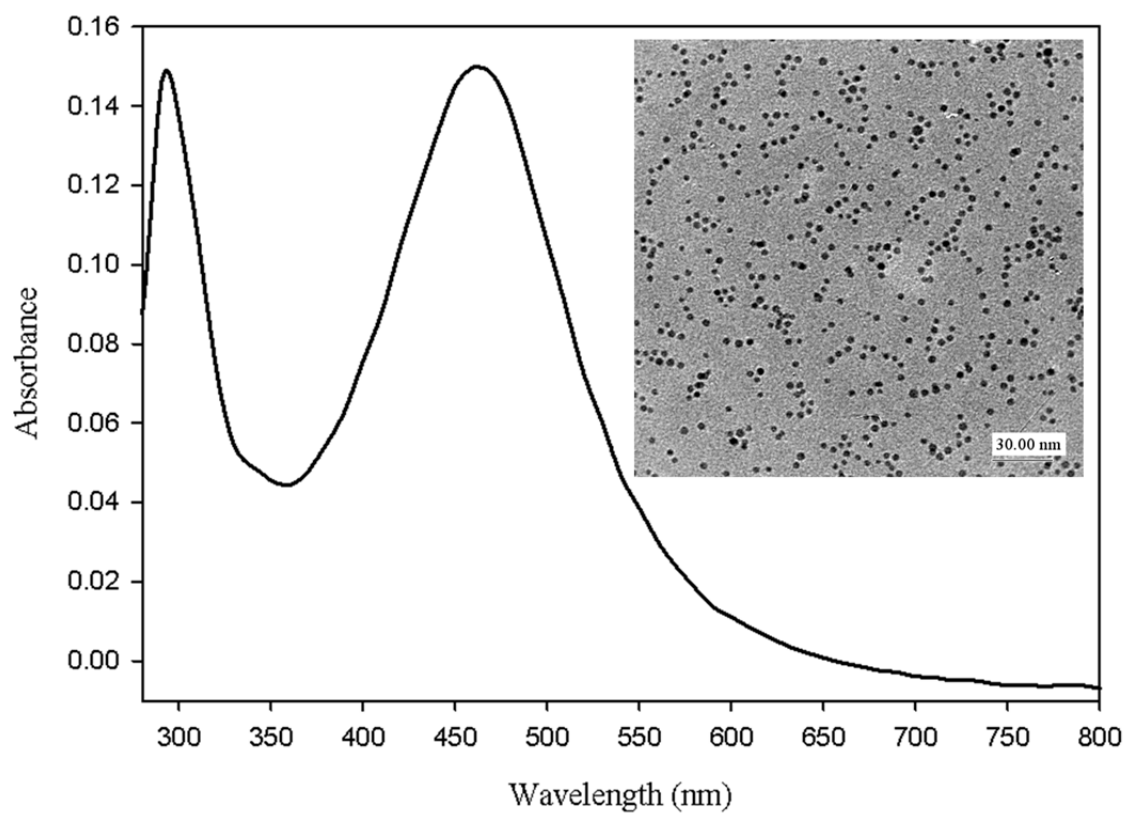
Figure 14. UV-VIS spectrum of R=108:S=12 Ag nanoparticles with TEM inset. The absorbance peak at $\lambda_{spr}\approx450$ nm signifies the presence of small Ag nanoparticles in toluene. The peak at $\lambda_{abs}\approx300$ nm is attributed to the *in-situ* formation of didodecyl disulfide. The TEM image confirms the presence of uniform spherical nanoparticles with D=3.8±1.7 nm.

4.3 Didodecyl Disulfide Synthesis and Characterization

To identify the absorbance peak at $\lambda_{abs}\approx300$nm in Figures 13 and 14, the procedure of Abbot and Hendrick was adapted to synthesize didodecyl disulfide.[53] The solid recovered from this reaction was dissolved in toluene and a UV-VIS spectrum was taken, which appears in Figure 15.
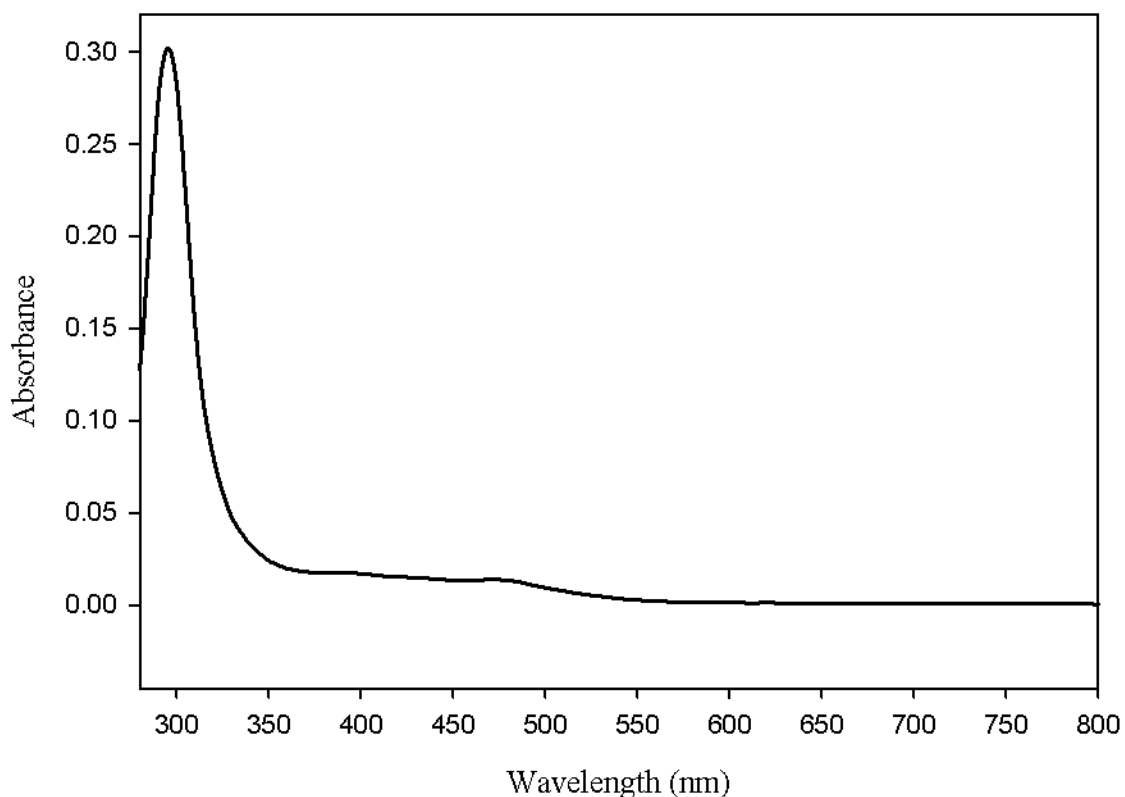
Figure 15. A UV-VIS spectrum of didodecyl disulfide dissolved in toluene. The strong, narrow absorbance peak at $\lambda_{abs}\approx300$nm matches that in Figures 13 and 14.

As Figure 15 shows an absorbance peak at $\lambda_{abs}\approx300$ nm which matches up well with that in Figures 13 and 14, it appears likely that the origin of the peak is didodecyl disulfide. To ascertain the formation of dodecanethiol, the following two control experiments were performed in which dodecanethiol was first dissolved in ethanol along

with NaBH$_4$. The mixture remained clear, indicating no didodecyl disulfide formation. Second, a similar test was carried out with AgNO$_3$ and dodecanethiol in ethanol. The formation of insoluble silver thiolates was observed, however, UV-VIS spectra taken from this test were featureless. As such, it appears that the Ag nanoparticles themselves catalyze the oxidation of thiols to disulfides.

Though didodecyl disulfide is likely present, Whiteside and colleagues report that disulfides and thiols have similar properties with respect to SAM formation,[51] meaning that disulfide formation may not impact nanoparticle growth. To test this, a sample of Ag nanoparticles was synthesized in which didodecyl disulfide was substituted for 1-dodecanethiol in an otherwise standard R=12:S=12 synthesis as in Figure 7. This sample was characterized with TEM; a representative image is reproduced in Figure 16.

The diameter of the nanoparticles synthesized with didodecyl disulfide is D=3.7±2.3nm, which is similar in size to those reacted with dodecanethiol that are on average are roughly D≈4.0±2.0nn as extracted from the nanoparticle uniformity region of Table 3. Hence, neither the final nanoparticle size nor polydispersity change if didodecyl disulfide is used as capping agent. Therefore, the *in-situ* formation of didodecyl disulfide should not significantly affect synthetic outcomes, and the development of a synthetic scheme to eliminate didodecyl disulfide formation appears unnecessary. To summarize, didodecyl disulfide likely forms in our reaction mixture under high reducing agent levels, but didodecyl disulfide appears not to affect the final nanoparticle size or polydispersity.
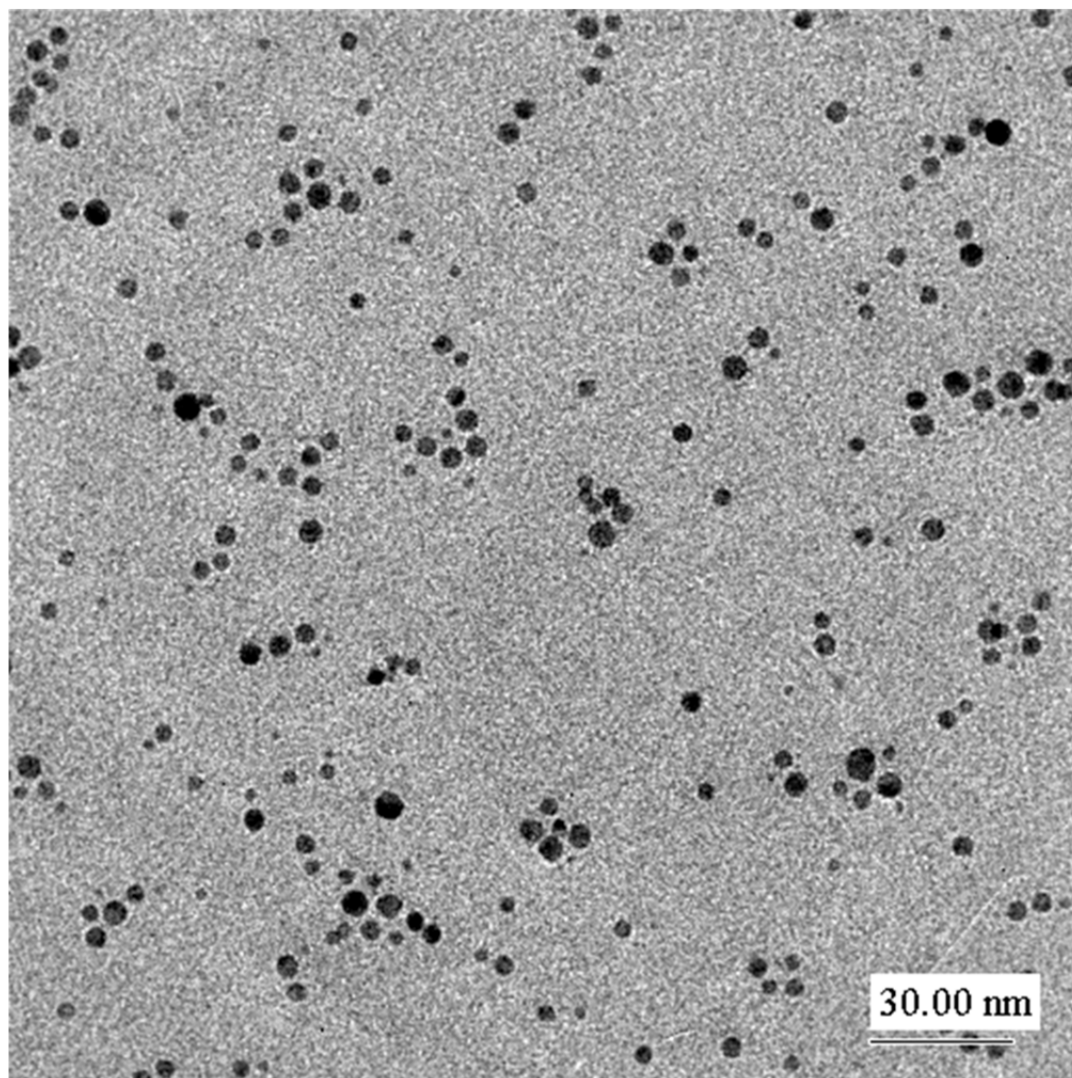
Figure 16: TEM image of Ag nanoparticles synthesized with didodecyl disulfide as capping agent. The average nanoparticle diameter for this sample is D=3.7±2.3 nm. Thus, neither the average particle size nor the standard deviation change due to the replacement of didodecyl disulfide for 1-dodecanethiol.

4.4 Discussion of Results

The following discussion is broken down into three parts, each addressing a specific aspect of our findings as it relates to our hypotheses. First, we consider the battery of the R=3-12:S=1-12 samples with respect to stabilizing the nanoparticles at early reaction times with dodecanethiol. Second, we elucidate the effect of high [NaBH$_4$], or high R, to test our hypothesis that steric interactions can stabilize nanoparticles in the absence of electrostatic repulsions. Third, we observe the sample synthesized with didodecyl disulfide standing in for dodecanethiol to validate our postulate that the final nanoparticle product would not be adversely affected.

Our first results from the battery of 16 samples cover a wide range of [NaBH$_4$] and [DDT] at constant [AgNO$_3$]. From the TEM images in Figures 7-9, the particle size and polydispersity data in Table 3, and the contour plots in Figure 10 and 11, three particle growth regimes emerge: the first at low [NaBH$_4$] at R=3 in the leftmost column of Figure 7; the second at low [DDT] at S=1 in the bottommost row of Figure 7; and the third with R>3 and S>1 in the remaining portion of Figure 7. In the R=3, or low reducing agent regime, particle size distributions were very polydisperse, with most samples having essentially a bimodal distribution. In this regime, the possibility exists that [NaBH$_4$] is too low to effectively drive the nucleation; Zukoski and coworkers drew similar conclusions with respect low reducing agent concentrations.[15] In the low dodecanethiol, or S=1 regime, particle distributions were also bimodal. The findings in this regime dovetail nicely with our predictions regarding the impact of steric interactions on colloidal stability at early reaction times, where on the basis of our surface coverage

calculations in Figure 5, it appears likely that the [DDT] was too low to cap all of the primary particles before aggregation.

In the third regime – the region of nanoparticle uniformity, Figures 7-11 and Table 3 show a transition to colloidal stability where spherical, uniform Ag nanoparticles of diameter, $D \approx 4.0 \pm 2.0$ nm form at intermediate [NaBH$_4$] and [DDT], corresponding to samples with $R \geq 6$ and $S \geq 3$. This finding indicates sufficient levels of dodecanthiol adsorb to the surface at early reaction times to stabilize primary particles through steric interactions. This outcome supports our hypothesis regarding the importance of having sufficient [DDT] to promote dense brush formation during early stage nucleation.

In the second part of the discussion, our findings at high [NaBH$_4$] with R=72-108 help to illuminate our second hypothesis, namely that electrostatic interactions do little to assist colloidal stability during early stage growth. This finding is illustrated in Figures 13 and 14, which show that uniform, spherical nanoparticles still form at extreme ionic strengths at which electrical double layer collapse is expected. Moreover we extrapolate from this finding that the reducing agent ratio to make uniform spherical Ag nanoparticles can be expanded to roughly two-orders of magnitude from $R \geq 6$-108.

Finally, the sample produced by synthesizing Ag nanoparticles in the presence of didodecyl disulfide rather than dodecanthiol assists in our assertion that in-situ formation of disulfides is not a major concern with respect to producing small, uniform Ag nanoparticles. Though we have yet to postulate the exact mechanism of *in-situ* didodecyl disulfide formation, it does not appear to affect the formation of the resulting functionalized nanoparticles. This position is also supported by the observations of Whitesides and coworkers with respect to the formation of SAMs on metallic surfaces.[51]

In summary, our hypothesis that steric interactions are essential at primary particle sizes to achieve colloidal stability, our hypothesis that the electrostatic interaction does little to stabilize primary particles against aggregation, and our postulate that the formation of didodecyl disulfide does not appreciably affect the final uniformity or size of our nanoparticle product have all been borne out by our findings. These successes demonstrate that it is possible to apply insight gained from the mechanisms of nanoparticle nucleation and growth through aggregation to design a straightforward, one-step synthetic method for the production of alkanethiol functionalized Ag nanoparticles.

5. Conclusions

The objective of this thesis was to develop a straightforward, one-phase synthesis for small, uniform, alkanethiol functionalized spherical Ag nanoparticles. To permit design of a new synthetic method, rooted in a rational exploration of the underlying processes of nucleation and aggregative growth, the reaction system was examined through the lenses of classical nucleation theory and colloidal stability paired with Derjaguin, Lendau, Verwey, Overbeek (DLVO) theory. In addition to demonstrating that it would be possible to stabilize the nanoparticles near the primary particle size, our calculations also indicated that with a properly structured synthesis, the change in stability with varying salt concentration (R) is extremely small. This led us to hypothesize that it would be possible to stabilize the nanoparticles near the primary particle diameter of $D{\approx}2$ nm, even in the absence of meaningful electrostatic stabilization.

To test our hypotheses and the effectiveness of our proposed synthetic method, a battery of 16 samples of Ag nanoparticles was synthesized. R-values ($R=[NaBH_4]/[AgNO_3]$) used were 3, 6, 9, and 12. S-values ($S=[DDT]/[AgNO_3]$) used were 1, 3, 6, and 12. Additionally, two samples were synthesized with R-values of 72 and 108, both paired with an S-value of 12. The results of these syntheses were characterized with transmission electron microscopy (TEM) followed by ImageJ image analysis and UV-VIS spectroscopy.

In general, our method produced small, uniform Ag nanoparticles, as long as R-values$\geq$6 and S-values$\geq$3 were used. As an example of the size and dispersion achieved, the $R=12$:$S=12$ synthesis produced nanoparticles with an average diameter of 4.7±1.6 nm. For the samples synthesized with elevated salt concentration, i.e. $R=72$ and $R=108$, the

resultant nanoparticles were not appreciably affected by the excess of salt in solution, having diameters of 3.5±0.8 and 3.8±1.7 nm, respectively. This demonstrably supports our hypothesis that nanoparticles do not gain appreciable stability from electrostatics and are instead stabilized by steric forces from the self-assembled monolayer brush. Finally, any concerns about unknown byproducts during synthesis have addressed via the synthesis, characterization, and usage of didodecyl disulfide as a capping agent during nanoparticle synthesis.

In summary, this work represents a new method for the production of small, uniform, functional Ag nanoparticles by exploiting the underlying physical processes of nanoparticle nucleation and aggregative growth. Future work which follows from and complements this thesis work will be addressed in the next section.

6. Future Work

The future work that stems from this thesis is focused on the final goal of producing uniformly-grafted and patchy polymer-grafted Ag nanoparticles for use in polymeric materials. To achieve this goal, there are a number of critical objectives as well as some complementary objectives. This section briefly discusses how each potential future objective relates to the overall theme of our work.

In order to grow polymer from the surface of a nanoparticle via atom transfer radical polymerization (ATRP), it is necessary to have a tethered ligand which possesses a moiety that can serve as an initiation site. Tertiary α-bromoesters commonly find application in this role. In addition to the bromoester, we also require the ATRP-active ligands to possess either a thiol or disulfide moiety, leading to material needs which are extremely specialized. This renders the possibility of purchasing them from commercial sources impractical. We have been able to synthesize and characterize an acceptable ATRP-active ligand possessing a disulfide moiety, however, purification of the crude product is still presenting somewhat of a challenge. Recently, we have made progress with a recrystallization technique from cold methanol, but it remains to be seen if this is a tenable solution in the long term.

Once we are confident of our ability to reliably produce and purify ATRP-active ligands with thiol or disulfide moieties, the synthetic techniques used to produce nanoparticles in this thesis will be applied to the production of nanoparticles with mixed ligand layers. Changes to the experimental techniques outlined here are expected to be minimal; 1-dodecanethiol will simply be replaced with the ligand or ligands of interest. Initial particle characterization to determine size will be carried out via TEM. Additional

characterization techniques will be brought to bear with the intention of determining SAM morphology. Existing techniques which have found application in this area include scanning tunneling microscopy (STM), matrix-assisted laser desorption/ionization time-of-flight mass spectroscopy (MALDI-TOF), Fourier transform infrared spectroscopy (FTIR), two-dimensional nuclear magnetic resonance spectroscopy (2D NMR), and atomic force microscopy (AFM). In addition to the existing techniques in this area, we are working on developing a novel application of energy filtered TEM (EFTEM) imaging which offers the possibility to produce real-space elemental maps of the nanoparticle SAM. This technique would be a welcome addition to the current arsenal of techniques available for characterization of nanoparticles with mixed SAMs.

In addition to progressing directly towards our final goal of producing polymer grafted nanoparticles, we also would like to round out the understanding that we have developed of the synthetic technique outlined in this paper. To do this, we are currently studying the effect that ligand length has on colloidal stability. This work complements the colloidal stability based synthetic approach outlined in this thesis nicely, as it will allow further comparison of our calculations of steric stability to experimental results. Finally, we have also begun experimenting with substitution of other ligands possessing thiol moieties for 1-dodecanethiol in our synthetic technique. These other nanoparticle variants allow us to gain valuable experience prior to attempting to produce nanoparticles functionalized with ATRP-active ligands. In addition, these nanoparticles serve as a convenient test bed for developing the aforementioned EFTEM techniques.

In short, development of a straightforward, one-phase technique for producing small, uniform, Ag nanoparticles has put us well on our way towards achieving our final

goal of being able to produce polymer grafted nanoparticles with phase-separated ligand monolayers. We are currently finalizing our techniques for production of pure ATRP-active ligands and are developing our skill with existing techniques for SAM characterization while also working towards the development of new techniques. In addition, we are attempting to exploit our insights into the underlying nucleation and growth mechanisms to their greatest potential by continuing to probe the reaction system with varied ligand lengths and functionalities. We intend to bring all of the knowledge and skill gained from these endeavors to bear on the final goal of producing polymer grafted nanoparticles with phase-separated ligand monolayers.

7. References

1. F. Hussain, M. Hojjati, M. Okamoto and R. E. Gorga, (2006). Polymer-matrix Nanocomposites, Processing, Manufacturing, and Application: An Overview, *Journal of Composite Materials,* 40, 1511-1575.

2. R. Sardar, A. M. Funston and R. W. Mulvaney, (2009). Gold Nanoparticles: Past, Present, and Future, *Journal of Surfaces and Colloids,* 25, 13840-13851.

3. S. Magdassi, A. Bassa, Y. Vinetsky and A. Kamyshny, (2003). Silver Nanoparticles as Pigments for Water-Based Ink-Jet Inks, *Chem. Mater.*, 15, 2208-2217.

4. T. VonWerne and T. E. Patten, (2001). Atom Transfer Radical Polymerization from nanoparticles: A Tool for the Preparation of Well-Defined Hybrid Nanostructures and for Understanding the Chemistry of Controlled/"Living" Radical Polymerizations from Surfaces, *J. Am. Chem. Soc.,* 123, 7497-7505.

5. M. McEwan, S. Egorov, J. Ilavsky and D. L. Green, (2011). Mechanical Reinforcement of Polymer Nanocomposites: Theory and Ultra-Small Angle X-Ray Scattering (USAXS) Studies, *Soft Matter,* 7, 2725.

6. C. Singh, P. K. Ghorai, M. A. Horsch, A. M. Jackson, R. G. Larson, F. Stellacci and S. C. Glotzer, (2007). Enropy-mediated patterning of surfactant-coated nanoparticles and surfaces, *Physical Review Letters*, 99, 22.

7. A. M. Jackson, Y. Hu, P. J. Silva and F. Stellacci, (2006). "From Homoligand to Mixed Ligand Monolayer-Protected Gold Nanoparticles: A Scanning Tunnelling Microscopy Investigation," *J. Am. Chem. Soc.*, 128, 11135-11149.

8. K. M. Harkness, A. Balinski, J. A. McLean and D. E. Cliffel, (2011) Nanoscale Phase Segregation of Mixed Thiolates on Gold Nanoparticles, *Angew. Chem. Int. Ed.*, 50, 10554-10559.

9. Egorov, S. A. (2012). Microphase separation of mixed polymer brushes physisorbed on cylindrical surfaces. Soft Matter, 8(14), 3971.

10. Nie, Z., Fava, D., Rubinstein, M. and Kumacheva, E., (2008). "Supramolecular" Assembly of Gold Nanorods End-Terminated with Polymer "Pom-Poms": Effect of Pom-Pom Structure on the Association Modes, *Journal of the American Chemical Society,* 130(11), 3683-3689.

11. Green, P., (2011). The Structure of Chain End-Grafted Nanoparticle/Homopolymer Nanocomposites. *Soft Matter*, 7, 7914-7926.

12. Sunday, D., S. Curras-Medina, and D.L. Green, (2010) Impact of Initiator Spacer Length on Grafting Polystyrene from Silica Nanoparticles. *Macromolecules*, 43, 4871-4878.

13. Huang, C., T. Tassone, K. Woodberry, D. Sunday, and D.L. Green, Impact of ATRP initiator Spacer Length on Grafting Poly(methyl methacrylate) from Silica Nanoparticles. *Langmuir*, 2009. 25.

14. Pyun, J., T. Kowalewski, and K. Matyjaszewski, Polymer Brushes by Atom Transfer Radical Polymerization, in Polymer Brushes, R. Advincula, W.J. Brittain, K.C. Caster, and J. Ruhe, Editors. 2004, Wiley-VCH: Weinheim. p. 35 - 68.

15. Hyning, D. L. V., & Zukoski, C. F. (1998). Formation Mechanisms and Aggregation Behavior of Borohydride Reduced Silver Particles. *Langmuir*, (20), 7034-7046.

16. Polte, J., Tuaev, X., Wuithschick, M., Fischer, A., Thunemann, A. F., Rademann, K., Kraehnert, R., et al. (2012). Formation Mechanism of Colloidal Silver Nanoparticles: Analogies and Differences to the Growth of Gold Nanoparticles. *ACS nano*.

17. Brust, M., Walker, M., Bethell, D., Schiffrin, D. J., & Whyman, R. (1994). Synthesis of thiol-derivatised gold nanoparticles in a two-phase Liquid-Liquid system. *Journal of the Chemical Society, Chemical Communications*, (7), 801.

18. Kimling, J., Maier, M., Okenve, B., Kotaidis, V., Ballot, H., & Plech, a. (2006). Turkevich method for gold nanoparticle synthesis revisited. *The Journal of Physical Chemistry B*, 110(32), 15700-7.

19. Bois, L., Chassagneux, F., Battie, Y., Bessueille, F., Mollet, L., Parola, S., Destouches, N., et al. (2010). Chemical growth and photochromism of silver nanoparticles into a mesoporous titania template. *Langmuir*, 26(2), 1199-206.

20. Shon, Y.-S., & Cutler, E. (2004). Aqueous synthesis of alkanethiolate-protected Ag nanoparticles using Bunte salts. *Langmuir*, 20(16), 6626-30.

21. Goulet, P. J. G., & Lennox, R. B. (2010). New Insights into Brust- Schiffrin Metal Nanoparticle Synthesis. *Journal of the American Chemical Society*, 132, 9582-4. ACS Publications.

22. Van Hyning, D. L., Klemperer, W. G., & Zukoski, C. F. (2001). Silver Nanoparticle Formation: Predictions and Verification of the Aggregative Growth Model. *Langmuir*, 17, 3128-3135.

23.   Adamson, A. W.; Gast, A. P. Physical Chemistry of Surfaces, Sixth Edition; John Wiley & Sons: New York, 1997.

24.   Chou, K., Chang, Y., & Chiu, L. (2012). Studies on the Continuous Precipitation of Silver Nanoparticles. *Industrial and Engineering Chemistry*, 51, 4905-4910.

25.   Lu, J., Dreisinger, D., & Cooper, W. (1997). Cobalt precipitation by reduction with sodium borohydride. *Hydrometallurgy*, 45, 305–322.

26.   Robb, D. T., & Privman, V. (2008). Model of Nanocrystal Formation in Solution by Burst Nucleation and Diffusional Growth. *Langmuir*, 2, 26-35.

27.   de Gennes, P.G., (1980) Conformation of Polymers Attached to an Interface. *Macromolecules*, 135, 1069.

28.   Alexander, S., (1977) Adsorption of Chain Molecules with a Polar Head a Scaling Description. *Le Journal de Physics*, 38, 983.

29.   D.H Napper, (1977) Steric stabilization, *Journal of Colloid and Interface Science*, 58, 390-407.

30.   Russel, W. B.; Saville, D. A.; Schowalter, W. R. Colloidal Dispersions, Cambridge University Press: Cambridge, 1999.

31.   M. Borowko, Computational Methods in Surface and Colloid Science, Marcel Dekker, New York, 2000.

32.   J. K. G. Dhont, An Introduction to the Dynamics of Colloids, Elsevier, Amsterdam, 2003.

33.   Kim, S., Karrila, S. J., Microhydrodynamics: Principles and Selected Applications, Butterworth-Heinemann, Stoneham, MA, 1991.

34.   Hiemenz, P. C.; Rajagopalan, R. Principles of Colloid and Surface Chemistry, Third Edition; Marcel Dekker, Inc: New York, 1997.

35.   Berg, J. C. An Introduction to Interfaces & Colloids: The Bridge to Nanoscience; World Scientific Publishing Co. Pte. Ltd: Hackensack, 2010.

36.   Lee, K. (1998). A closer look at an aggregation model of the Stöber process. Colloids and Surfaces A: Physicochemical and Engineering Aspects, 144, 115-125.

37.   Kitchens, C., & McLeod, M. (2003). Solvent effects on the growth and steric stabilization of copper metallic nanoparticles in AOT reverse micelle systems. *The Journal of Physical Chemistry B*, 107, 11331-11338.

38.   Schulze, H. (1882). Schwefelarsen im wässeriger Lösung. *J. Prakt. Chem.* **25,** 431 52.

39.   Schulze, H. (1883). Antimontrisulfid im wässeriger Lösung. *Z. Phys. Chem.* **92,** 129 68.

40.   Hardy, W. B. (1900) A preliminary investigation of the conditions which determine the stability of irreversible hydrosols. *Proc. Roy. Soc. Lond.* **66,** 110-25.

41.   Freundlich, H. (1910). Die Bedeutund der Adsorption bei der Fallung der Suspensions kolloide. *Z. Physik. Chem.* **73,** 385-423.

42.   Derjaguin, B. V. and Landau, L. (1941). Theory of the stability of strongly charged lyophobic sols and the adhesion of strongly charged particles in solutions of electrolytes. *Acta Physicochim. URSS* **14,** 633-62.

43.   Verwey, E. J. and Overbeek, J. Th. G. (1948). *Theory of the Stability of Lyophobic Colloids.* Elsevier.

44.   Hogg, R., Healy, T. W. and Fuerstenau, D. W. (1966). Mutual coagulation of colloidal dispersions. *Far. Soc. Trans.* **62,** 1638-51.

45.   Adler, P. M. (1981). Heterocoagulation in shear flow. *J. Colloid Interface Sci.* **83,** 106-15.

46.   Vincent, B., Edwards, J. Emmett, S. and Jones, A. (1986). Depletion flocculation in dispersions of sterically-stabilised particles ("soft spheres"), *Colloids and Surfaces*, 18, 261-281.

47.   Ohshima, H. (1995). Electrostatic interaction between 2 dissimilar spheres with constant surface charge density. *J. Colloid Interface Sci.* 174, 45.

48.   Nallathamby, P. D., Lee, K. J., & Xu, X.-H. N. (2008). Design of stable and uniform single nanoparticle photonics for in vivo dynamics imaging of nanoenvironments of zebrafish embryonic fluids. *ACS nano*, 2(7), 1371-80.

49.   Dutta, N. and D.L. Green. (2008) Nanoparticle Dispersion in Semidilute and Concentrated Polymer Solutions. Langmuir, 24, p. 5260-5269

50.   Dutta, N. and D.L. Green. (2010). Impact of Solvent Quality on Nanoparticle Dispersion in Semidilute and Concentrated Polymer Solutions. Langmuir, 26, p. 16737-16744.

51.   Love, J. C., Estroff, L. a, Kriebel, J. K., Nuzzo, R. G., & Whitesides, G. M. (2005). Self-assembled monolayers of thiolates on metals as a form of nanotechnology. *Chemical reviews*, 105, 1103-69).

52.   Goulet, P. J. G., & Lennox, R. B. (2010). New Insights into Brust- Schiffrin Metal Nanoparticle Synthesis. *Journal of the American Chemical Society*, 132(28), 9582-4.

53.   Shah, R. R., Merreceyes, D., Husemann, M., Rees, I., Abbott, N. L., Hawker, C. J., & Hedrick, J. L. (2000). Using Atom Transfer Radical Polymerization To Amplify Monolayers of Initiators Patterned by Microcontact Printing into Polymer Brushes for Pattern Transfer. *Macromolecules*, 33(2), 597-605.

54.   Chaki, N. K., Sharma, J., Mandle, a. B., Mulla, I. S., Pasricha, R., & Vijayamohanan, K. (2004). Size dependent redox behavior of monolayer protected silver nanoparticles in aqueous medium. *Phys. Chem. Phys.*, 6(6), 1304.

55.   Singh, S., Chaturvedi, J., Bhattacharya, S., & Nöth, H. (2011). Silver(I) catalyzed oxidation of thiocarboxylic acids into the corresponding disulfides and synthesis of some new Ag(I) complexes of thiophene-2-thiocarboxylate. *Polyhedron*, 30(1), 93-97.